Interface investigation and engineering – achieving high performance polymer photovoltaic devices†‡

Li-Min Chen,§[a] Zheng Xu,§[b] Ziruo Hong[a] and Yang Yang[a]

Received 2nd December 2009, Accepted 12th January 2010
First published as an Advance Article on the web 26th February 2010
DOI: 10.1039/b925382c

The contact between the polymer active layer and the electrode is one the most critical interfaces in polymer solar cells. In this article, we report the progress of interface engineering in polymer solar cell research, where the multiple functions of the interfacial materials will be discussed. The vertical composition profile in polymer:fullerene blends is an emerging topic, and the interlayer effect on the vertical phase separation and device performance will be highlighted. We also discuss the energy level alignment at the bulk heterojunction (BHJ) interface, with the aim of providing a better understanding towards the route of high efficiency polymer solar cells.

1. Introduction

Recent progress in polymer photovoltaics, has led to reports of power conversion efficiencies (PCEs) reaching 6–7%.[1–5] In addition, the scalability and compatibility with flexible, large-area substrates affirms polymer solar cells for high throughput, low cost renewable energy alternatives to their inorganic counterparts. The advancement of record-high PCEs is driven by the synthesis of novel donor and acceptor materials, implementation of innovative interfacial materials, and adoption of revolutionary processing conditions. In the bulk heterojunctions (BHJs), the inevitable potential loss due to the energy level offset between the donor and acceptor renders the electrode contacts a critical factor to derive the net potential out of the BHJs. It is therefore necessary to establish ohmic contacts at both electrodes for efficient charge extraction, which is challenging for interfaces between organic/polymer and metals. An interface with a barrier height of a few tens of mV may result in significant charge accumulation, and thus significant recombination loss and inferior photovoltaic (PV) performance. Consequently, the interface between the BHJ and both the anode and cathode is of fundamental importance to the charge transport and extraction process, which determines the device performance and long term stability. Tremendous efforts have been devoted to elucidate and engineer the interface since the evolution of polymer solar cells. Particularly in solution-processed polymer active layers, the surface properties of the bottom interface have a substantial influence on the film morphology, while the BHJ morphology grown above can be manipulated accordingly.

In this article, we shall highlight common interfacial materials employed at the anode and cathode of polymer solar cells. An overview of the functional interlayers will be provided. Both the

[a]*Department of Materials Science and Engineering, University of California, Los Angeles, Los Angeles, CA 90095, USA*
[b]*Solarmer Energy, Inc., 3445 Fletcher Ave, El Monte, CA 91731, USA*

† This paper is part of a themed issue of *Journal of Materials Chemistry* on Interface engineering of organic and molecular electronics, guest edited by Alex Jen.

‡ The authors gratefully acknowledge financial support from the Air Force Office of Scientific Research (Grant No. FA9550-07-1-0264), Office of Naval Research (Grant No. N00014-04-1-0434), Solarmer Energy Inc., University of California Discovery Grant, and NSF IGERT: Materials Creation Training Program (MCTP) (DGE-0114443) and the California Nano-Systems Institute (CNSI).

§ Contributed equally to this work.

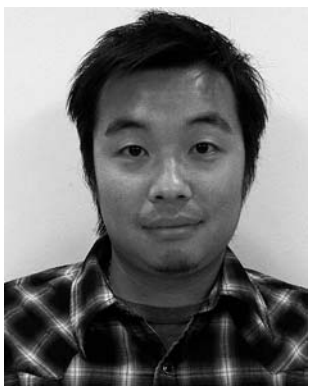

Li-Min Chen

Li-Min (Raymond) Chen has been a Ph.D. student in Prof. Yang Yang's group in the Department of Materials Science and Engineering at the University of California, Los Angeles since 2006. He obtained his B.S. and M.S. from National Cheng Kung University (Taiwan) in 2002 and 2004, respectively. His research focuses on polymer solar cells with novel structures and processing methods as well as transparent conductor applications.

Zheng Xu

Zheng Xu is a Senior Researcher at Solarmer Energy, Inc. in El Monte, CA. He obtained his Ph.D. in Materials Science and Engineering at the University of California, Los Angeles in 2009, focusing on organic electronic devices and their interfaces (advisor: Prof. Yang Yang). Before he entered UCLA, he received his B.S. (2000) and M.S. (2003) in Physics at Fudan University (China). His current research focus is on polymer solar cells.

lateral and vertical phase morphologies are critical to the device performance, but only recently has the vertical phase morphology acquired immense attention. The vertical phase morphology is essential to the charge transport and collection process since the photoactive layer is sandwiched between the two electrodes. We will discuss the effect of the interface property on the film morphology, mainly in the vertical direction, and report methods on controlling the vertical composition gradient. The last part will focus on the energy alignment at the BHJ/electrode interfaces.

2. Interfacial materials

2.1 Functions of interfacial materials

The metal/organic interface plays an essential role in determining the overall device performance of organic electronics, and inserting a functional interfacial layer can dramatically alter the interface properties. The main functions of the interfacial layer include:

(1) Minimization of the energy barrier for charge injection and extraction. In OLED/PLEDs, the injection efficiency of carriers dramatically depends on the barrier height at the metal/organic interface, where the tunneling current is inversely proportional to the barrier height.[6] In this sense, it is intuitive to lower the barrier height by engineering the interface contacts. In polymer solar cells, it is rather important to understand whether the open-circuit voltage (V_{OC}), which relates to the built-in electric field for charge extraction, is determined by the intrinsic properties of the BHJ system (V_{OC1}), or the choice of metal electrodes (V_{OC2}), as illustrated in Fig. 1.[7] For non-ohmic contacts, the V_{OC} follows the metal–insulator–metal (MIM) model, which equals the work function difference of the electrodes. On the other hand, charge transfer leads to the Fermi level alignment for ohmic contacts, and the work function of the cathode and anode is pinned to the lowest unoccupied molecular orbital (LUMO) of the acceptor and the highest occupied molecular orbital (HOMO) of the donor, respectively, determining the V_{OC}. In this case, band bending at the ohmic contact reduces the V_{OC} (Fig. 2), whereas charge recombination at the donor/acceptor interface governs the V_{OC} of the BHJ device.[8–12] More recently, the formation of charge transfer excitons (CTEs) between the polymer and fullerene has shown strong correlation with the V_{OC}, providing insight to its origin, as well as suggested routes to approach the theoretical V_{OC}.[11,13–16]

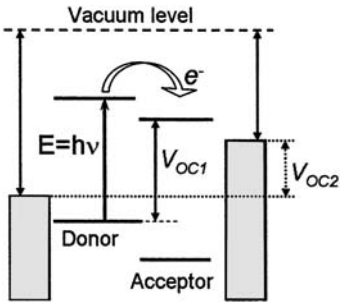

Fig. 1 Schematic variation of V_{OC} with the acceptor strength (V_{OC1}) and/or electrode work function (V_{OC2}) in a BHJ solar cell device. (Reprinted with permission from ref. 7; copyright 2003, American Institute of Physics.)

(2) Formation of a selective contact for single types of charge carrier. Charge selectivity at the electrode interfaces is crucial to ensure effective charge extraction by blocking the charge carrier flow towards the unfavored direction. Interfacial layers of wide bandgaps can serve as an exciton-blocking layer (EBL) to eliminate the parasitic exciton quenching at the metal/organic interface.[17–20] Furthermore, certain interfacial layers allow the selective transportation of either electrons or holes, such as an electron-transporting layer (ETL) with hole-blocking properties, and a hole-transporting layer (HTL) with electron-blocking properties. These functional interfacial layers can significantly improve the charge selectivity at the electrodes,[21–23] and have been widely implemented in OLED/PLEDs, and excellent reviews can be found in the articles by Hung and Chen[24] and Walzer *et al*.[25]

Ziruo Hong

Ziruo Hong obtained his B.S. in Chemistry from Sichuan University, 1995, and Ph.D. in physics from Changchun Institute of Optics, Fine Mechanics and Physics, Chinese Academy of Sciences in 2001. He has been working on device design and mechanism study of organic electroluminescence and photovoltaics in Hong Kong, Singapore and Germany. He is currently working on polymer solar cells, especially solar cells with stacking structures, in Prof. Yang Yang's group at UCLA. His main research interest is focused on organic opto-electronics, especially light emitting devices and photovoltaic cells. He has published over 70 research papers on international journals.

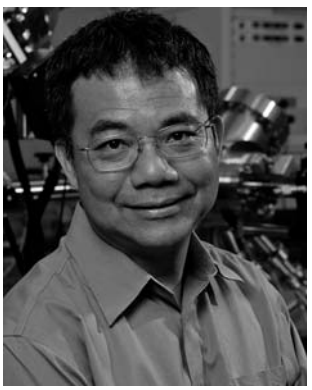

Yang Yang

Originally from Taiwan, Prof. Yang received his Ph.D. degree in Physics and Applied Physics at the University of Massachusetts, Lowell. After working at the University of California, Riverside as a postdoctoral researcher, and in the UNIAX Corporation as a research staff member, he joined the University of California, Los Angeles in 1997. He has been a full professor at UCLA since 2002. His group is working on solution processable electronic devices, including organic and inorganic solar cells, organic LED and memory devices, and carbon-based nanomaterials. He has published more than 170 articles in peer-reviewed journals.

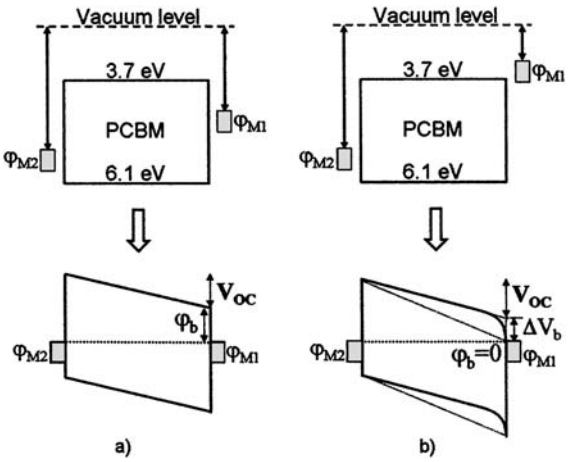

Fig. 2 Schematic band diagram of a metal–insulator–metal (MIM) device with (a) non-ohmic and (b) ohmic contacts for electrons and holes. Before (upper image) and after contact (lower image) under short-circuit conditions. φ_b and ΔV_b are the injection barrier height for electrons at a non-ohmic contact and the voltage loss at an ohmic contact, respectively. φ_{M1} and φ_{M2} are work functions of the metal contacts. (Reprinted with permission from ref. 7; copyright 2003, American Institute of Physics.)

(3) Determination of the relative polarity of the devices. In principle, ITO is capable of collecting either electrons or holes since its work function (*ca.* 4.5–4.7 eV) lies between the typical HOMO and LUMO of common organic photovoltaic (OPV) materials. Accordingly, the polarity of ITO can be modified to efficiently collect either electrons or holes by coating with functional interlayers of different work functions.[26] Device polarity is thus controlled by the relative positions of functional interlayers with various work functions, irrespective of the conducting electrodes, as shown in Fig. 3. Metals with various work functions can also be employed as either cathode or anode *via* selecting suitable interlayers. The versatility of ITO establishes the foundation of the inverted structure solar cell, which also exhibits the potential advantage of improved lifetime and preferred vertical composition gradient.[27–29]

(4) Modification of the surface property to alter film morphology. The substrate surface property is capable of manipulating the film morphology due to the surface-directed spinodal decomposition, particularly during the spin-coating process of the polymer blend films.[30–32] Modifying the substrate surface property with various self-assembled monolayers (SAMs) can alter the molecular preference and arrangement at the film/substrate interface, and therefore affect the contact properties, such as barrier height and available charge transfer sites, as well as the vertical phase morphology.[28,29,33,34]

(5) Suppression of diffusion and reaction between the electrode material and polymer. A detrimental effect of metal ion diffusion into the organic layer is substantial leakage current.[35,36] The chemical reaction at the metal/organic interface can also vary the contact properties, forming interfacial dipole barriers and defect states that pin the Fermi level. The kink/hump (s-shape) observed in certain current density–voltage (*J*–*V*) curves is speculated to arise from the interface barriers.[37,38] Therefore, an inert buffer layer that prevents the diffusion and reaction at this interface is desired.

(6) Modulation of the optical field as an optical spacer. The BHJ active layer is typically sandwiched between two electrodes, where one is transparent and the other reflective. The incident light forms a standing wave inside the active layer. The optical field intensity diminishes to zero at the polymer/reflecting electrode interface, while the maximum intensity is located at a certain distance away from the reflective mirror, depending on the refractive indices and thickness of the active layer. An optically transparent spacer can redistribute the electric field and push the absorbing region away from the interface to a higher electric-field strength, which enhances the short-circuit current (J_{SC}), as shown in Fig. 4.[4,39,40] Optical spacers have been shown to be most effective for thin active layers limited by low carrier mobilities, whilst not so useful for films of optimal film thickness.[41,42]

2.2 Overview of interfacial materials

In the last twenty years extensive efforts have been devoted to OLED/PLED research and a variety of functional interfacial

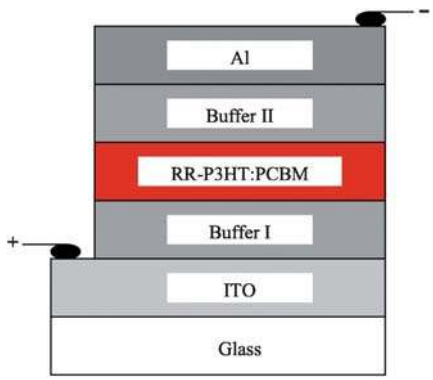

Fig. 3 The device structure of a polymer solar cell, where the device polarity can be controlled by the relative position of the functional buffer layers. (Reprinted with permission from ref. 26; copyright 2006, American Institute of Physics.)

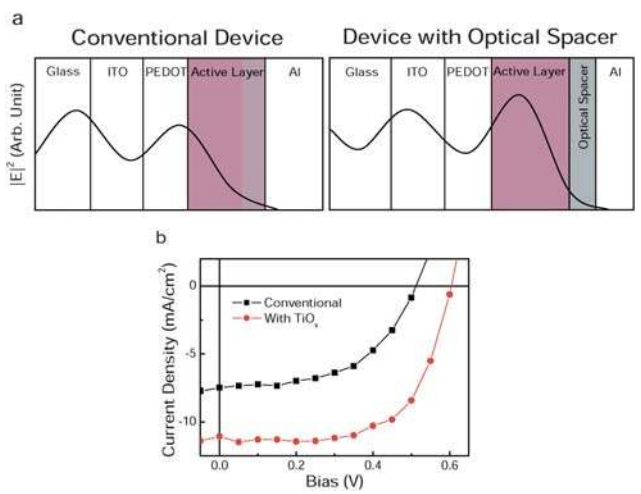

Fig. 4 (a) Schematic representation of the spatial distribution of the squared optical electric-field strength $|E|^2$ inside the devices with a structure of ITO/PEDOT/active layer/Al (left) and ITO/PEDOT/active layer/optical spacer/Al (right). (b) The current density–voltage characteristics of polymer solar cells with (●) and without (■) the TiO_x optical spacer under AM 1.5 illumination. (Reprinted with permission from ref. 39; copyright 2006, Wiley VCH.)

materials have been developed,[24] and also successfully transferred to engineer the interfaces in polymer solar cells with promising results. This article will provide an overview of the most prominent interfacial materials in polymer solar cell applications. The interfacial materials implemented at both the cathode and anode interfaces will be separately discussed within three main categories, namely inorganic salts, inorganic semiconducting oxides, and organic and self-assembled monolayers (SAMs).

2.2.1 Cathode interlayers. It is preferable for the cathode interface to have a low work function contact for efficient electron extraction. While Al and Ag are the most common electrode materials, the thermal evaporation process frequently alters the quality of the metal/organic interface.[43,44] The reactive hot metal atoms can lead to chemical interaction at the interface and diffusion into the organic layer.[45,46] It should be noted that alternative approaches are also capable for the cathode deposition, such as spray-coating of Ag nanoparticles and transferring of Ag nanowire meshes.[47,48] Lögdlund *et al.*[49] and Antoniadis *et al.*[50] suggested that the instability of the Al electrode is related to the Al–C bond formation, which interrupts the π-conjugated system. Therefore, other low work function metals such as Ca, Mg, and Ba, are often employed to protect the metal/organic interface, while being capped by the Al or Ag electrode.

The low work function metal Ca has been used to improve device performance since the development of polymer diodes.[1,51,52] For poly(3-hexylthiophene):[6,6]-phenyl-C_{61}-butyric acid methyl ester (P3HT:PCBM) blend-based solar cells with an Al cathode, a dipole layer pointing from Al to PCBM exists at the PCBM/Al interface, which increases the charge extraction barrier and reduces the V_{OC}.[7,53] Inserting Ca between the Al electrode and the polymer forms an ohmic contact that results in a high fill factor (FF).[54] The thin n-doped layer induced by Ca deposition pins the surface energy level at the polymer/metal interface, which facilitates the charge transport.[55] Ca reacts with water at room temperature, while being relatively inert to molecular oxygen.[56] Nonetheless, the instabilities of Ca and Mg in ambient atmosphere require combining with metals with a low permeation rate to moisture such as Al and Ag to form effective cathodes. In a recent study, low work function bilayer electrodes such as Ba/Al and Ca/Al show superior device performance than higher work function electrodes (Table 1).[57]

Table 1 Detailed current density–voltage (J–V) characteristics for various top electrodes. Literature work function (Φ) values are listed for the metal contacting the active metal. (Reprinted from ref. 57; copyright 2008, American Institute of Physics)

Electrode	Work function (eV)	V_{OC} (mV)	J_{SC} (mA/cm^2)	FF (%)	Normalized efficiency
Ag	4.26	403 ± 27	9.04 ± 1.16	36.6 ± 3.7	0.36 ± 0.08
Al	4.28	420 ± 15	10.02 ± 0.33	38.2 ± 2.6	0.41 ± 0.03
Mg:Ag/Ag	3.66	565 ± 6	10.30 ± 0.39	50.5 ± 2.8	0.75 ± 0.06
LiF/Al	2.9	580 ± 2	10.42 ± 0.22	57.3 ± 1.2	0.89 ± 0.03
Ca/Al	2.87	601 ± 2	10.42 ± 0.18	60.6 ± 2.1	0.96 ± 0.04
Ba/Al	2.7	600 ± 2	10.47 ± 0.36	62.2 ± 1.5	1.00 ± 0.04

Alkali metal compounds, including LiF,[58–60] CsF,[61] Cs_2CO_3,[62–64] CsCl,[65] as well as 8-hydroxyquinolinolato lithium (Liq)[66] and other organic metal complexes,[67] typically provide low work function contacts, and are commonly used as the electron injection layer in OLED/PLEDs. Alkali metal acetates also deliver similar results.[68] Among these functional compounds, LiF and Cs_2CO_3 have found the most success in polymer solar cells.

The introduction of a bilayer cathode composed of LiF/Al and MgO/Al can enhance electron injection due to band bending of the organic layer in contact with the insulating layers.[58] By inserting LiF or other compounds (oxides and halides) of group IA and IIA metals between Al and tris-8-hydroxyquinoline aluminium (Alq_3), a better contact is also formed.[69,70] LiF was adapted to polymer solar cells to facilitate electron extraction, and resulted in significant device improvement for the poly-(2-methoxy-5-(3′,7′-dimethyl-octyloxy))-*p*-phenylene vinylene (MDMO-PPV):PCBM blend, where the V_{OC} and FF increased to 0.82 V and 61%, respectively.[71] The function of the LiF layer was suggested to arise from either dipole formation at the Al/LiF/polymer interface[70,72] or the LiF buffer protection.[73] Jönsson *et al.* reported the thickness-dependence of LiF, where for (sub)monolayer coverage, Al deposition decomposes LiF, causing Li-doping of the organic material to yield a low work function contact,[74] while thicker LiF creates a dipole layer that downshifts the work function.[75] Other fluorides such as CsF,[61] CaF_2,[69] MgF_2,[76] NaF,[77] and KF,[78,79] were also reported to exhibit similar phenomena. A comparative study between LiF, NaF, and KF showed that the variation in reverse current density is caused not only by interface modification but also by diffusion and doping of the whole organic layer, which depends on the interlayer thickness.[80] NaF was suggested as an alternative choice due to the minimum thickness requirement.

Caesium carbonate (Cs_2CO_3) is another promising electron injection material.[62–64,81,82] The function of Cs_2CO_3 is rather versatile and insensitive to the cathode material, where thermal evaporation or spin-coating the Cs_2CO_3 layer, as well as using either Al or Ag as the electrode, deliver comparable performances.[82] The actual product of thermally-evaporated Cs_2CO_3, either doped caesium oxide or caesium carbonate molecules, has been under debate.[82–87] Nonetheless, the formation of a low work function Al–O–Cs complex upon Al deposition facilitates electron extraction in polymer solar cells and electron injection in PLEDs.[82] Inserting a 1 nm Cs_2CO_3 layer between the active layer and the Al increases both the V_{OC} and FF.[26] Chen *et al.* reported similar results with improvement to 3.1% PCE due to the reduced series resistance (R_s).[88] A 2.1% PCE semitransparent polymer solar cell was also fabricated with a 70% transparency cathode composed of Cs_2CO_3 (1 nm)/Ag (7 nm)/ITO (100 nm). The device performance was further improved to 2.8% by placing a reflective Ag mirror behind the device to compensate for light loss.[89] While 0.5 Å of Cs_2CO_3 is sufficient to lower the electron injection barrier into Alq_3, a minimum thickness of 10 Å is required to convert the ITO surface to a low work function cathode for the inverted structure.[85] Modification of the ITO polarity for inverted structure and their performance will be discussed in the next section.

Transparent semiconducting metal oxides such as TiO_2 are commonly employed as an electron acceptor and transport

material because of its processability and non-toxicity, as well as wide applications in dye sensitized solar cells and photocatalysts.[90–92] TiO_2 is a robust diffusion barrier against oxygen and water due to its scavenging effects originating from photocatalysis and oxygen deficiency.[90,93] Relatively air-stable polymer solar cells and LEDs have been demonstrated by incorporating the TiO_x layer.[94] Fig. 5 illustrates a device structure incorporating the TiO_x layer, as well as how this layer prevents the permeation of oxygen and moisture. The flow chart also shows the preparation steps of the TiO_x layer.

Generally, crystalline TiO_2, either in the anatase or rutile phase, requires a heat treatment process above 450 °C that is incompatible with polymer devices. For the practical use of low cost polymer PV devices, it is essential to fabricate functional oxide layers with compatible solution processes. Kim *et al.* reported a low temperature sol–gel process to fabricate a titanium oxide layer (Fig. 5).[39] A spin-coated precursor solution converts to a 30 nm titanium oxide film by hydrolysis in air at room temperature, and a transparent amorphous titanium oxide film was obtained after annealing at 150 °C for 10 min. XPS study revealed an oxygen-deficient TiO_x film, where Ti:O = 1:1.34. The TiO_x film exhibited an electron mobility approximately 1.7×10^{-4} cm^2 V^{-1} s^{-1}, and a LUMO level of 4.4 eV, close to the work function of Al, rendering it an efficient electron-transport material. The large band gap of the TiO_x film (*ca.* 3.7 eV) is capable of blocking the holes and excitons efficiently. In addition, the TiO_x layer serves as an optical spacer to spatially redistribute the light intensity inside the device (Fig. 4a).[4,39,40,95] The TiO_x optical spacer substantially enhances both the external quantum efficiency (EQE) and J_{SC} (Fig. 4b) by approximately 40% compared to devices without the optical spacer and a 5% PCE was achieved in P3HT:PCBM BHJ devices. Hayakawa *et al.* also reported substantial device enhancement for a TiO_x layer atop the active layer, but with only a small increase in J_{SC}.[22] Due to the excellent hole-blocking property of TiO_x, the enhancement in shunt resistance (R_{sh}) and rectification ratio contributed to the improvement in both V_{OC} and FF, while the TiO_x layer also functions as a barrier against physical damage and chemical degradation. Recently, a 6.1% PCE was reported for poly[*N*-9″-hepta-decanyl-2,7-carbazole-alt-5,5-(4′,7′-di-2-thienyl-2′,1′,3′-benzothiadiazole):[6,6]-phenyl C_{71}-butyric acid methyl ester (PCDTBT:PC_{70}BM) BHJ device by inserting a TiO_x layer, with an internal quantum efficiency (IQE) approaching 100% around 450 nm.[4] Such a high IQE value indicates the high efficiency of converting absorbed photons into charge carriers that are collected at the electrodes. However, in the case of additive incorporation, the optical spacer effect counteracts with the additive concentration, *i.e.* the nanoscale roughness.[95]

Incorporation of dopants and varying processing are common methods to modify the metal oxide properties.[96–98] We reported Cs-doped TiO_2 (TiO_2:Cs) by mixing Cs_2CO_3 solution with a nanocrystalline TiO_2 solution synthesized *via* a non-hydrolytic sol–gel process.[99] Cs lowers the TiO_2 work function such that the TiO_2:Cs interfacial layer improves the polymer/metal contact, as well as provides excellent electron extraction and hole-blocking properties to deliver a PCE of 4.2%. The versatile functionality of the TiO_2:Cs layer was also extended to PLEDs with similar improvement. Fig. 6 shows that the TiO_2:Cs interfacial layer delivers better performance compared to either TiO_2 or Cs_2CO_3 alone in both PV devices and PLEDs.

Solution-process high efficiency polymer tandem cells using TiO_x and poly(3,4-ethylenedioxythiophene):poly(styrene

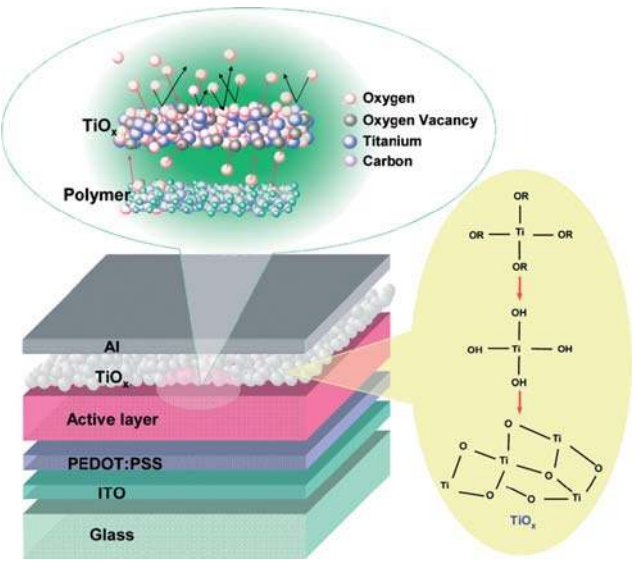

Fig. 5 The device architecture with the TiO_x layer, as ITO/PEDOT:PSS/active layer/TiO_x/Al. The TiO_x layer functions as a scavenging layer to block the permeation of oxygen and moisture into the polymer active layer. The brief flow chart shows the preparation steps of the TiO_x. (Reprinted with permission from ref. 94; copyright 2007, Wiley VCH.)

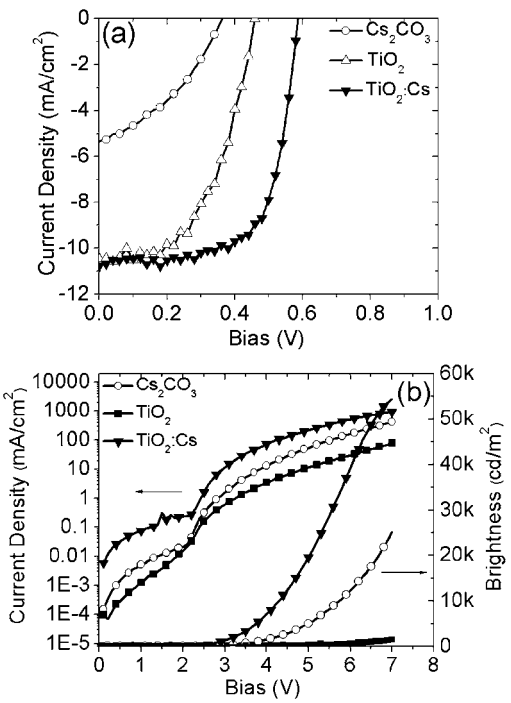

Fig. 6 (a) Current density–voltage characteristics of a P3HT:PC_{70}BM BHJ device with an evaporated Al cathode and different interfacial layers. (b) Current density–voltage–brightness characteristics for a PLED device with different interfacial layers. (Reprinted with permission from ref. 99; copyright 2009, Wiley VCH.)

sulfonate) (PEDOT:PSS) as the interlayer were successfully demonstrated with a 6.5% PCE.[100] The TiO_x layer functions as the electron transport and collecting layer for the front sub-cell as well as the foundation of the rear sub-cell, where the PEDOT:PSS layer serves as the hole-transport layer (HTL). We also reported implementing pristine TiO_2 and TiO_2:Cs in a tandem cell based on P3HT:$PC_{70}BM$ and poly[(4,4′-bis(2-ethylhexyl)dithieno[3,2-*b*:2′,3′-*d*]silole)-2,6-diyl-*alt*-(2,1,3-benzothiadiazole)-4,7-diyl] (PSBTBT):$PC_{70}BM$ BHJs, with a PCE of 5.84%.[101,102] The TiO_2/PEDOT:PSS (4083) interconnecting layer behaves as a Schottky contact, where exposure to UV light increases the free carrier concentration in TiO_2 which leads to efficient electron tunneling through the energy barrier.[103] Fig. 7a shows the necessity of UV light illumination to the TiO_2 layer, where a significant hump (s-shape) was observed with the UV cutoff filter. It was also pointed out that extra care should be taken to avoid under-estimating the device area when using high conductivity materials in the interlayer, such as PH500 (Fig. 7b).

Another solution-processable n-type metal oxide is ZnO, which has a high electron mobility of 0.066 $cm^2\ V^{-1}\ s^{-1}$.[104] ZnO also shows a similar optical spacer effect for thin active layers, which is less pronounced for thick films.[41] This indicates that the optical spacer effect might be particularly advantageous for thin films limited by low carrier mobilities, but not for films of optimal film thickness.[39,42] The first polymer tandem cell using a solution-processed interlayer was realized with a combination of ZnO nanoparticles and neutral PEDOT.[105] Neutral PEDOT was used since acidic PEDOT dissolves the ZnO nanoparticles.

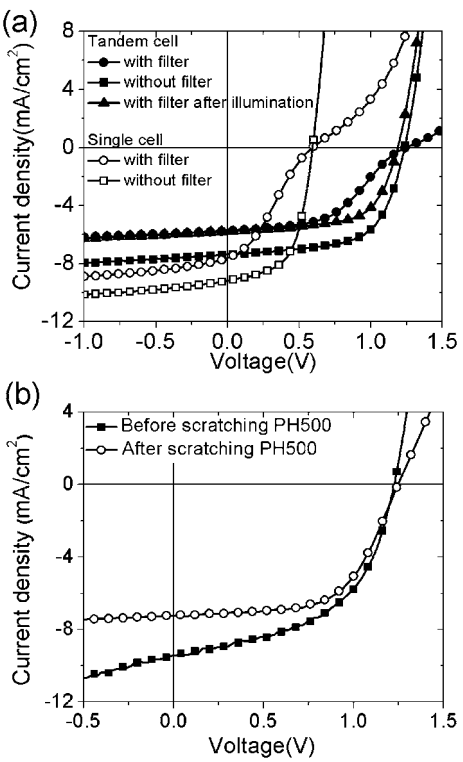

Fig. 7 (a) Current density–voltage characteristics of single and tandem cells under illumination with and without a 400 nm cutoff filter. (b) A tandem cell using PH500 as an interlayer before and after defining the active area by scratching. (Reprinted with permission from ref. 102; copyright 2009, Wiley VCH.)

The charge recombination at the interlayer was improved by n-doping (photo-doping) the ZnO layer by exposure to UV light,[106,107] where incorporating metallic clusters also exhibits similar effects.[108]

Modifying the ITO surface with SAMs with permanent dipole moments can alter the work function and surface property to improve the device performance. SAMs with electron withdrawing groups increases the ITO work function, while electron donating groups reduce it.[109] However, the resulting phase separation was reported to be a more dominating factor than matching the energy levels. Khodabakhsh *et al.* utilized SAMs to improve both hole injection and charge collection, pointing out that SAM-modified electrodes can affect the subsequent film morphology and the density of active sites for charge collection.[33,110] SAMs can also be used in combination with functional metal oxides, such as TiO_2 and ZnO, to further improve the interface properties. Systematic studies of modifying the TiO_2/BHJ interface showed that SAMs can improve the interface *via* several mechanisms, including: reducing charge recombination, passivating inorganic surface states, providing additional exciton dissociation interface, and influencing the BHJ composition distribution for better charge selectivity.[111,112] Alkanethiol SAMs were shown to increase the J_{SC} for hybrid P3HT-ZnO solar cells from 0.28 to 0.42 mA/cm^2 despite their insulating nature. The enhanced J_{SC} was due to the increased crystallinity of the interfacial P3HT, which can be attributed to larger exciton diffusion length, hole mobility, or reduced electron–hole recombination rate.[113–115] Interface modification with SAMs of different dipole directions and chemical bondings can significantly improve the contact properties of the ZnO/metal bilayer cathode, where stable high work function metals, such as Ag and Au, can also be used as cathodes.[116,117] Modifying the ZnO surface with a benzoic acid (BA) group decorated with a negative dipole (such as $–OCH_3$ or $–CH_3$ end groups), which points toward the ZnO layer (away from the metal), decreases the band offset and facilitates the ohmic contact formation. A cathode with a ZnO/BA–OCH_3/Al configuration exhibited a 4.2% PCE compared to 3.2% from the unmodified cathode. Modification of the ZnO with a mercaptoundecanoic acid (MUA) SAM further improved the efficiency to 4.6%.[116]

Reports on organic interfacial material in polymer solar cells have been scarce, despite their wide application in OLEDs and small molecule solar cells.[25] Poly(ethylene oxide) (PEO) was shown to enhance the V_{OC} up to 200 mV, possessing the similar function as LiF, but with the advantage of solution processability.[118] Ionic liquid-functionalized carbon nanoparticles (ILCNs) play a similar role to lower the electron collection barrier at the cathode.[119] A thin layer of alcohol/water-soluble polyelectrolyte can improve the V_{OC} up to 0.3 V due to superposition of the interfacial dipole upon the built-in electric field.[120] Alcohol-soluble polyfluorene derivatives as the cathode buffer layers also show similar device performance improvement.[121,122]

2.2.2 Anode interlayer. PEDOT:PSS has been commonly used to improve the anode contact with ITO.[123] Spray deposition of a thick PEDOT:PSS layer (*ca.* 1.2 μm) as the top electrode has been demonstrated with a PCE of 2%.[124] However, its acidic nature etches the ITO and imposes potential lifetime instability.[125–127] Rutherford backscattering (RBS) studies showed

that the ITO/PEDOT:PSS interface is not stable, where indium diffuses into the PEDOT:PSS. XPS also confirmed the dissolution of ITO in PEDOT:PSS. Furthermore, previous studies revealed PEDOT:PSS to be an inefficient electron-blocking layer due to electron leakage at the anode.[126,128]

Two criteria must be taken into consideration for an efficient anodic buffer layer to replace PEDOT:PSS. The fabrication compatibility must be guaranteed to withstand the organic solvent exposure. Furthermore, the surface properties of the anodic buffer layer have a significant impact on the molecular ordering and phase separation process of the BHJ active layer, which must be considered as well. A few transition metal oxides (MoO_3, V_2O_5, and WO_3) are highly transparent and conductive, and have been successfully employed to modify the anode interface. In addition to replacing PEDOT:PSS for the ITO/polymer contact, these transition metal oxides have particularly found applications in the inverted structure polymer solar cells, since they can be easily evaporated on top of the polymer active layer. We will first discuss the hole collection properties of these transition metal oxides in the regular device structure, followed by their applications in the inverted structure.

Shrotriya *et al.* reported replacing PEDOT:PSS with V_2O_5 and MoO_3 as the anodic interlayer.[129] Fig. 8 compares the device performance of PV devices with various anode interlayers, where optimum thicknesses of V_2O_5 (3 nm) and MoO_3 (5 nm) exhibit comparable performances ($3.2 \pm 0.1\%$ PCE) to PEDOT:PSS. An optimized metal oxide thickness is critical: too thin a layer leads to a lower V_{OC} and leakage current due to incomplete coverage, while too thick a layer increases the series resistance (R_s) and reduces the J_{SC} and FF. Insertion of a MoO_3 interlayer improves the device performance for both small molecule and polymer solar cells.[130,131] The band bending at the interface leads to enhanced hole extraction which decreases R_s, and is more pronounced for small molecules, since PEDOT:PSS already forms an excellent ohmic contact for polymer solar cells. Interestingly, the V_{OC} of the tetraphenylporphine (H2TPP)/C_{60} system increased linearly from 0.57 to 0.97 V as the MoO_3 thickness increased from 0 to 50 nm, which can be attributed to the enhanced built-in potential without the occurrence of Fermi lever

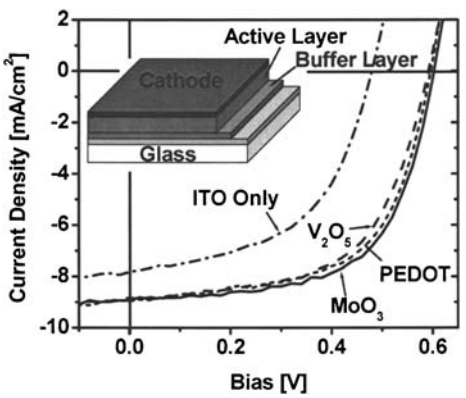

Fig. 8 Current density–voltage characteristics of PV devices under illumination with different anode interlayers, namely, ITO only, ITO/PEDOT:PSS (25 nm), ITO/V_2O_5 (3 nm), and ITO/MoO_3 (5 nm). (Reprinted with permission from ref. 129; copyright 2006, American Institute of Physics.)

pinning resulting from charge transfer. Furthermore, an Al/MoO_3 layer has been reported as the interconnection layer in tandem cells, where the MoO_3 layer (*ca.* 15 nm) protects the polymer active layer from subsequent solvent exposure.[132] By employing MoO_3 as the electron-blocking layer, the detrimental effect of the leakage current to V_{OC} was demonstrated, where a leakage current two orders of magnitude lower doubled the V_{OC} in small molecular solar cells.[133] WO_3 was reported to planarize the ITO surface and assist the ordering of P3HT.[134] In addition, WO_3 has been used as the hole-transport layer in combination with 4,7-diphenyl-1,10-phenanthroline (Bphen) as the electron-transport layer for a copper phthalocyanine (CuPc)/C_{60} device.[135] The device improvement was attributed to the higher work function of WoO_3, which is a better match with CuPc.

Despite successful anode interlayer alternatives, the semiconducting properties of these transition metal oxides are not yet fully understood. A recent report by Kröger *et al.* suggested the n-type nature of MoO_3 and WO_3, where hole injection results from electron extraction from the HOMO of the organic semiconductor to the conduction band (CB) of MoO_3.[136] Due to the various oxidation states of these transition metal oxides and their useful applications, the electronic nature of these metal oxides requires further in-depth investigation.

Insertion of a p-type NiO layer (5–10 nm thick) to replace PEDOT:PSS as the anode buffer layer can substantially enhance the P3HT:PCBM device performance to 5.2% with excellent device stability.[23] NiO has a work function of 5.0 eV, and essentially forms an ohmic contact with P3HT. It functions as a hole-transport and electron-blocking layer, where holes can be efficiently collected, and the large bandgap (*ca.* 3.6 eV) simultaneously provides high transparency and sufficient energy barrier for electron collection. The high V_{OC} of 0.638 V was attributed to this improved p-type NiO layer that reduces the leakage current.

Robust hole-transport layers were also introduced *via* an organosiloxane cross-linkable approach to replace PEDOT:PSS. Cross-linkable 4,4′-bis[(*p*-trichlorosilylpropylphenyl)phenylamino]-biphenyl ($TPDSi_2$) itself and blends with poly[9,9-dioctyl-fluorene-*co*-*N*-[4-(3-methylpropyl)]diphenylamine] (TFB) delivered better or comparable performances in both PLEDs and BHJ solar cells due to the improved hole-injection and electron-blocking ability.[128,137,138] Polytetrafluoroethylene (PTFE) also forms a dipole at the polymer/metal interface that decreases the energy barrier and thus facilitates hole extraction.[139] Sulfonated poly(diphenylamine) (SPDPA) was also shown to form an ohmic contact with P3HT and enhance its crystallinity and mobility.[140]

2.2.3 Inverted polymer solar cells. The polarity of ITO can be modified by coating with different functional interlayers to collect either electrons or holes (Fig. 3). The most common application is coating ITO with a high work function layer for hole collection, such as PEDOT:PSS. Li *et al.* demonstrated the ability to lower the ITO work function by an ultrathin Cs_2CO_3 layer such that it becomes the cathode to extract electrons.[26] Other prominent examples of the inverted structure include utilizing electron-transport layers with good hole-blocking properties, such as TiO_x and ZnO atop ITO.[21,141] The potential interface instability is overcome by replacing the acidic PEDOT:PSS, while the cathode can be substituted with either

PEDOT:PSS, which has excellent oxygen-blocking properties,[142] or other high work function materials.

Using a solution-processed titanium oxide of 10 nm as the electron-selective contact and PEDOT:PSS/Au as the anode delivered an inverted cell of 3.1% PCE.[21] The PEDOT:PSS solution was diluted in isopropanol and heated to 80 °C prior to spin-coating upon the hydrophobic polymer active layer. The reduced leakage current under reversed bias indicates the effective hole-blocking property of the TiO_x layer. *o*-Xylene instead of chlorobenzene (CB) was used as the solvent and the formation of a favorable morphology with improved vertical phase separation was suggested.[143] Polyoxyethylene tridecyl ether (PTE) improved the TiO_x precursor wetting to form a better contact, which results in a higher FF due to reduced R_s and increased R_{sh}.[144] Ameri *et al.* compared the regular and inverted structure by optical modeling, and attributed the higher EQE maximum of the inverted structure to the non-negligible absorption of the PEDOT:PSS layer.[145] However, no significant "optical spacer" effect of the TiO_x layer was observed in the inverted structure.

Incorporating ZnO on ITO as the cathode buffer layer with a silver anode delivers a PCE of 2.58%.[141] An almost 85% EQE maximum validates the excellent IQE and charge collection efficiency. Kyaw *et al.* fabricated inverted cells based on ZnO and MoO_3 interlayers.[146] The ZnO transmittance was controlled by the crystal size, which depends on the precursor concentration.[147] Relatively stable solar cells with a 3.5% PCE were obtained by using ZnO nanoparticles to modify the ITO substrate.[27] Modifying the ZnO nanoparticle surface with a C_{60}-SAM further improved the efficiency to 4.9%. The C_{60}-SAM passivates the surface traps of ZnO, and enhances the electronic coupling at the ZnO/organic interface, which suppresses the recombination losses. It was speculated that PCBM accumulation at the C_{60}-SAM interface benefits the high PCE since organic field effect transistor (OFET) measurements showed the accumulation of PCBM at the C_{60}-SAM-modified interface.[111]

An ultrathin Ca layer was also used as the electron-transport layer to modify the ITO, while an optimum thickness of MoO_3 served as the hole-transporting layer to prevent charge recombination at the Ag anode.[148] Interestingly, transition from regular to inverted device was reported due to oxidation of the silver top contact, where the work function changes from 4.3 to 5.0 eV upon oxidation.[149]

Vanadium oxide has various oxidation states and is reported to protect the polymer active layer and suppress the backward current at the PCBM/metal interface, as well as to prevent penetration of the hot metal atoms.[36,150] A 2.25% PCE inverted cell was fabricated by modifying the ITO surface with Cs_2CO_3, with V_2O_5/Al as the anode.[26] Semitransparent inverted devices were formed by replacing Al with 12 nm of Au. The PCE increased to 4.2% by annealing the Cs_2CO_3 layer at 150 °C for 20 min, which was attributed to the heavily-doped caesium oxide formation that reduces the interfacial resistance at the cathode.[87] Fig. 9 shows that the device performance increases with the annealing temperature of the Cs_2CO_3 layer until 150 °C, which also corresponds to the variation in contact angle of the Cs_2CO_3-modified surface with water. The inset shows the significant enhancement upon annealing at 150 °C. The improvement is also due to the beneficial vertical composition profile of the inverted structure, which will be discussed in the next section.[28,29]

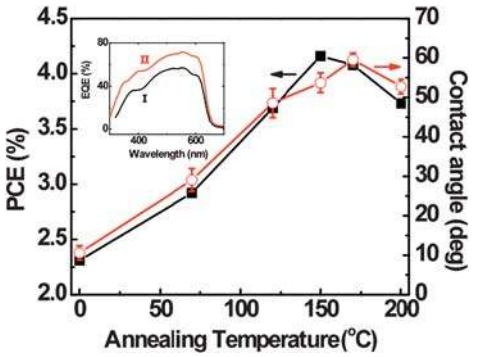

Fig. 9 Device efficiency and contact angle with water of the Cs_2CO_3 interlayer as a function of different annealing temperatures. The inset shows the effect of annealing treatment on the EQE. Line I is the Cs_2CO_3 layer without annealing, and line II is after 150 °C annealing. (Reprinted with permission from ref. 87; copyright 2008, American Institute of Physics.)

Ouyang and Yang reported that by incorporating D-sorbitol into PEDOT:PSS, a transparent "electric glue" can be formed, which is capable of laminating films together both mechanically and electrically.[151] Implementing the unique property of the electric glue into the inverted configuration, a semitransparent polymer solar cell based on the P3HT:PCBM blend was fabricated by the lamination process with a 3% PCE.[152] This method took advantage of the solution process, which also featured self-encapsulation and provided an alternative to the roll-to-roll production. A series of alkali metal compounds were evaluated, and revealed the formation of interface dipole layers at the ITO surface, which is shown in Fig. 10. The direction of the dipole moments points from the ITO surface to vacuum that reduces the

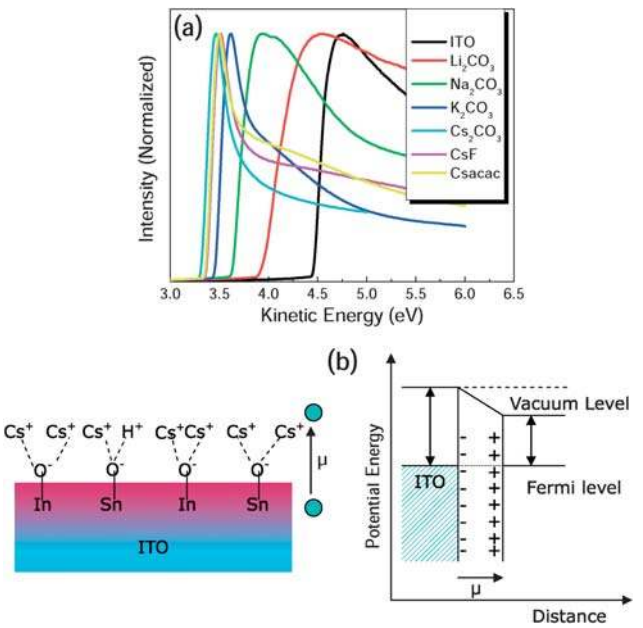

Fig. 10 (a) Variation of secondary electron edge with different buffer layers on ITO, (b) scheme for the formation of dipole layer on ITO and its effect on reducing the ITO work function. (Reprinted with permission from ref. 152; copyright 2008, Wiley VCH.)

ITO work function. The amount of the work function reduction is determined by the magnitude of the dipole moment, which correlates to the V_{OC} variation, and is proportional to the electron-donating ability of the alkali metal ions.

In order to fabricate transparent top electrodes, either thermal evaporation of very thin metal layers or sputter deposition of transparent metal oxides are required.[26,89,153–156] However, thin metal layers often suffer from transparency loss and low conductivity, while sputter deposition inevitably introduces damage to the polymer layer.[155,157] The inverted structure based on Cs_2CO_3 allows the formation of transparent cathodes, such as Cs_2CO_3/Ag/ITO, which was deposited on flexible metal foils and yielded a *ca.* 3% PCE.[158] Evidently, another application of transition metal oxides lies in protecting the polymer active layer during the sputtering process to form a semitransparent electrode, such as MoO_3/ITO.[159] Other examples include MoO_3/Ag/MoO_3, WO_3/Ag/WO_3, MoO_3/Al, which are employed in tandem or multiple-stacked cells.[132,153,160]

An ordered heterojunction that utilizes the ordered mesoporous architecture of inorganic materials possesses the advantage of controlled nanoscale phase separation, and defined pathways without dead ends to provide straightforward charge collection.[161] Coakley and McGehee demonstrated hybrid P3HT-titania ordered BHJ devices with a 0.5% PCE. Since then, nanotube arrays of TiO_2 and ZnO have been implemented to assist the charge transport for P3HT:PCBM blends in inverted cells, but the performance was still inferior to most regular device structures.[150,162–164] The typical small pore sizes of 10–20 nm are comparable to the exciton diffusion lengths of polymers, but result in rather random polymer chain packing instead of the high degree of π–π stacking.[165] The efficiency is thus limited by the poor alignment (crystallinity), low mobility, and insufficient infiltration of the polymer. Recently, Mor *et al.*[166] demonstrated a 4.1% PCE double heterojunction polymer solar cell *via* vertically oriented TiO_2 nanotube arrays, as illustrated in Fig. 11. By tailoring the pore sizes of the TiO_2 nanotubes, the infiltrated polymer chains self-aligned into aggregates according to the nanotube direction. It has been reported that the hole mobility can be enhanced 20 times by this vertical channel confinement-induced alignment.[165] Moreover, both polymer-fullerene and polymer-TiO_2 interfaces provided efficient charge separation, and the nanotube arrays prohibited charge recombination at the electrodes since simultaneous contact with both electrodes can be avoided. This double heterojunction device exhibited an EQE maximum of 80%, and a high J_{SC} of 12.4 mA/cm^2.

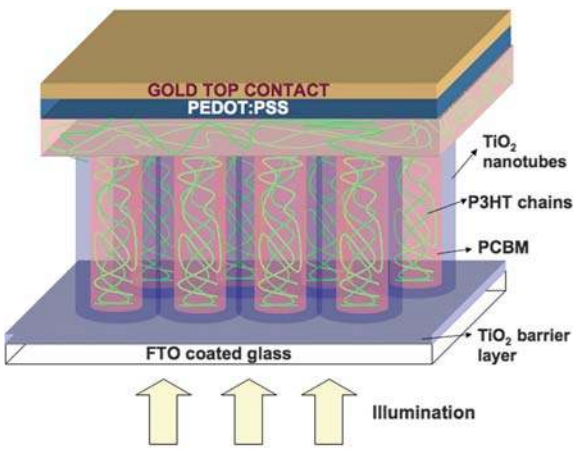

Fig. 11 Illustration of the double heterojunction polymer solar cells based on TiO_2 nanotube arrays. (Reprinted with permission from ref. 166; copyright 2007, American Institute of Physics.)

3. Vertical phase separation

3.1 Vertical phase separation in polymer blends

The film morphology evolution of polymer blends is a complex interplay governed by the phase-separation process and the interaction between the polymer components and the surface and substrate interface, where the final morphology is controlled by both thermodynamic and kinetic parameters. The rapid evaporation of the solvent freezes the film morphology into a non-equilibrium state, whereas relaxation toward the equilibrium state is often prohibited by kinetic barriers. Due to the low entropy of mixing, immiscible polymer blends tend to demix (phase-separate) upon spin-coating from their parent blend solutions, while surface effects and differences in surface energies have profound effects on the composition profile.[167] Surface properties have long been known to significantly impact the phase-separation morphology in binary polymer blends, while blend composition, polymer–substrate interaction, and interfacial tension all play crucial roles in determining the final film morphology.[168]

Theoretically, the composition in polymer blend films can be described as characteristic wave vectors $q_{\parallel}$ and $q_{\perp}$, which are parallel and normal to the substrate, respectively. When $1/q_{\perp}$ is comparable to the film thickness, vertical phase separation can be promoted by increasing $q_{\perp}$ from attracting one of the blend components to the surface *via* modifying the chemical structures or substrate properties.[30,169] Indeed, vertical-segregated blend films due to preferred interaction with the air interface and a more viscous solvent have been reported.[170] In this section, vertical phase separation in conventional and conjugated polymer blends will be introduced, as well as their applications in polymer electronics. The observations of vertical phase separation in two major polymer solar cell systems will be discussed, along with the utilization of this concept.

Experimentally probing the composition of polymer blend films was made possible by advances in depth profiling and imaging techniques. A comprehensive review can be referred to the article by Krausch.[171] Depth profiling techniques include forward recoil spectrometry (FReS) and nuclear reaction analysis (NRA), which are based on real space profiling, and neutron reflectivity (NR) and X-ray reflectivity (XRR), which are based on momentum space. Jones *et al.* showed experimentally surface-directed spinodal decomposition of a mixture of isotopic polymer poly(ethylenepropylene) (PEP) and perdeuterated poly(ethylenepropylene) (d-PEP), where preferential attraction leads to enrichment of d-PEP at the surface.[30] Fig. 12 shows that the surface is enriched with d-PEP, and a damped oscillation from the surface, the wavelength of which grows with the annealing time. Bruder and Brenn reported that the surface interaction can alter the spinodal decomposition process to form either a bilayer morphology or domain structures.[172] Krausch

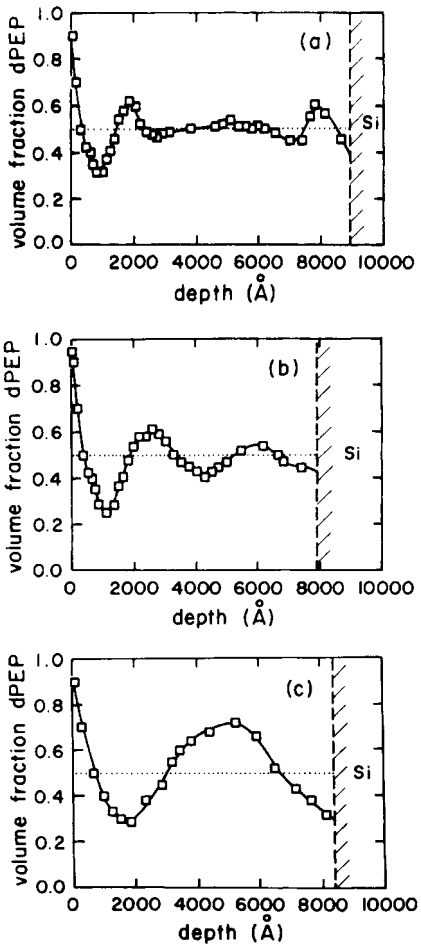

Fig. 12 Volume fraction *vs.* depth profiles of d-PEP in an initially uniform mixture with a d-PEP volume fraction of 0.5 after aging at 35 °C for (a) 19 200 s, (b) 64 440 s, and (c) 172 800 s. (Reprinted with permission from ref. 30; copyright 1991, The American Physical Society.)

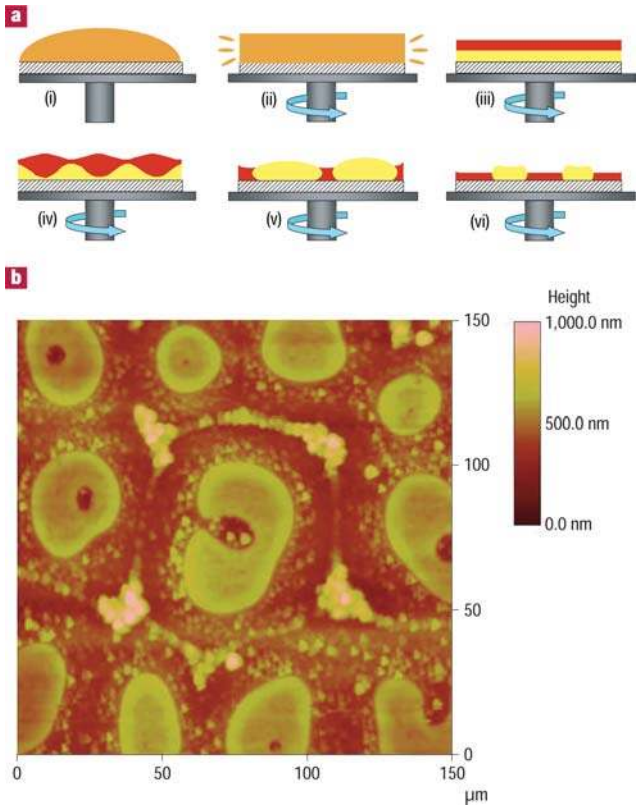

Fig. 13 A schematic model describing the film formation during the spin-coating process, and the final film morphology. (a) After the initial spin-off stage where both polymer and solvent are removed (i), (ii), the film separates into two layers (iii) and the film thins owing to solvent evaporation only. The interface between the polymers destabilizes (iv) and the film phase-separates laterally (v), (vi). (b) An atomic force microscope image of the final morphology. (Reprinted with permission from ref. 175; copyright 2005, Nature Publishing Group.)

et al. studied the thickness dependence of the spinodal decomposition process to the film composition, revealing interference effects from the two spinodal waves originating from the two distinct surfaces.[31] Walheim *et al.* revealed that the topography of polymer blend films is controlled by the solvent solubility and the substrate properties.[32] By properly tailoring these two parameters, either component in the immiscible polystyrene/poly(methyl methacrylate) (PS/PMMA) blend can be preferentially segregated at the substrate surface, where the film morphology can also show a complete phase inversion. Ton-That *et al.* reported surface enrichment of PMMA in various compositions of the PS/PMMA blend, and attributed the surface segregation to the different solubility of the polymers in the solvent and the relative dewetting of PMMA-rich domains from PS-rich phases.[173] Budkowski *et al.* demonstrated that the solvent evaporation rate depends on the substrate surface chemistry, which changes the convection process.[168] Concave and convex surface features were observed for blend films of polystyrene (PS) and polyisoprene (PI) spin-coated from toluene onto hydrophobic and hydrophilic SAM-modified substrates, respectively, while the overall morphology was similar. Böltau *et al.* showed that the phase-separated domains can form arbitrary structures with a concentration variation by patterning the surface with various SAMs.[174] Morphology evolution was studied *in situ* by time-resolved small-angle light scattering and light reflectivity.[175] The formation of the transient wetting layers at both the surface and substrate interfaces initiates from the vertical stratification, and the heterogeneous solvent evaporation causes a solvent concentration gradient, which leads to the interfacial (Marangoni-like) instability and eventually lateral phase separation. This film evolution process in spin-coating is illustrated in Fig. 13. Depending on the spin-coating parameters, the initial multilayer structures can either be "frozen"[168] or "broken up"[176] into lateral domains. Arias *et al.* also reported that by controlling the solvent evaporation rate, either self-stratified or lateral phase separated morphologies could be obtained.[177]

Besides conventional polymer blend systems, vertical phase separation has also been reported on a variety of semiconducting polymer systems, which possess important applications in organic electronics, such as LEDs and transistors. Chappell *et al.* utilized scanning near-field optical microscopy (SNOM) to identify the poly(9,9′-dioctylfluorene) (PFO) emission from the poly(9,9′-dioctylfluorene-altbenzothi-adiazole) (F8BT)-rich domains originating from the preferential wetting of the PFO

film (*ca.* 10 nm) at the surface.[178] Kim *et al.* studied the film morphology of (F8BT) and poly(2,7-(9,9-di-n-octylfluorene)-alt-(1,4-phenylene-((4-secbutylphenyl)imino)-1,4-phenylene)) (TFB) blend.[179] An enrichment of the low surface energy component (TFB) at both the air and substrate interfaces was observed as a result of interfacial-energy reduction. Due to the preferential wetting of the hole-transporting TFB layer at the substrate, PLEDs without a PEDOT:PSS layer with comparable efficiency were demonstrated. Higgins *et al.* reported the existence of a wetting layer for different composition ratio, and pointed out that a better solvent can impede its formation.[180] Both the composition ratio and the casting solvent have a significant effect on the PLED device performances, and different stages of the film morphology evolution can thus be obtained by controlling the solvent evaporation rate *via* substrate heating.[181,182]

Vertical segregation was also reported in P3HT blended with other semicrystalline polymers.[183] The sequential crystallization induced vertical stratification to occur in a "double-percolation-like" mechanism.[184] The film morphology results from successive phase separation processes, initially in the liquid phase, followed by segregation of the solidified P3HT, which is caused by the crystallization of the matrix component. The exothermic crystallization process drives the solidified semiconducting polymer to segregate toward the surface and interface, leading to a vertically phase-separated morphology. These vertically-stratified structures are particularly beneficial for FET applications, since transport of charge carriers only takes place at the gate dielectrics interface.[185] Utilizing this concept, only 3 wt% semiconducting polymer was required without compromising the performance.

By varying the substrate surface energy, PMMA can either segregate at the top surface to function as an encapsulation material or at the bottom surface as a dielectric layer.[186,187] Furthermore, the PSS-rich surface in the PEDOT:PSS blend has been identified,[188,189] while adding glycerol or D-sorbitol to the PEDOT:PSS solution prior to spin-coating increases the film conductivity due to aggregation of PEDOT-rich particles.[151,190]

3.2 Vertical phase separation in APFO-3:PCBM

The vertical phase separation plays a crucial role in the charge collection process of polymer solar cells, since the photogenerated charges must transport vertically to the sandwiching electrodes. Two polymer blend systems, namely polyfluorene and polythiophenes, blended with PCBM, have received considerable investigation regarding the vertical phase separation morphology to date.

Alternating polyfluorene copolymers (APFOs), with various donor–acceptor–donor segments, have been intensively studied for photoactive materials and achieved a PCE of 4.2%.[191,192] Jönsson *et al.* reported surface enrichment of poly[(9,9-dioctylfluorenyl-2,7-diyl)-*co*-5,5-(4′,7′-di-2-thienyl-2′,1′,3′-benzothiadiazole] (APFO-3), where the surface composition for a 1:4 blend ratio of APFO-3:PCBM was 1:1.[75] Dynamic secondary ion mass spectroscopy (SIMS) is an established technique to map the topographic and compositional profiles in both lateral and vertical directions, thus revealing the 3D morphology of polymer blend films.[193] Björström *et al.* utilized dynamic SIMS and observed a multilayer structure after spin-coating APFO-3:PCBM blends in chloroform for a range of blend ratios.[194] The vertical structure exhibited a four-fold multilayer morphology with APFO-3 enriched at the surface, followed by a PCBM-enriched layer underneath, then an APFO-3-enriched layer in the middle, and a PCBM-enriched (APFO-3-depleted) layer adjacent to the substrate. It was suggested that the self-stratification was due to composition waves caused by the surface-directed phase separation,[30] and if enough time was allowed to reach thermodynamic equilibrium, a bilayer structure instead of the frozen four-layer structure should eventually evolve. Recently, Björström *et al.* compared the photovoltaic performance of the APFO-3:PCBM blend of three various device structures: a vertically homogeneous layer, a diffusive bilayer, and a spontaneously formed multilayer, as illustrated in Fig. 14A–C.[195] The diffusive bilayer was formed by spin-coating PCBM dissolved in dichloromethane solution at high speed onto the polymer layer, whereas APFO-3 was partially dissolved by exposure to dichloromethane.[196,197] By selecting a solvent with a desired volatility (evaporation rate), homogeneous or multilayer

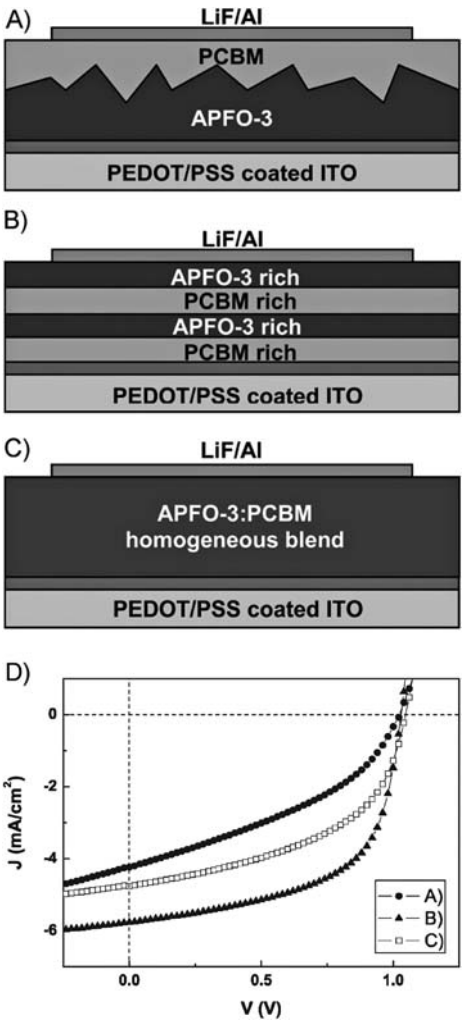

Fig. 14 Schematic illustration of the solar cells with active layers based on APFO-3 and PCBM with: (A) diffuse bilayer morphology, (B) spontaneously formed multilayer structure, and (C) homogenous blend morphology. (D) The corresponding *J–V* characteristics under white light illumination for the 3 device morphologies. (Reprinted with permission from ref. 195; copyright 2009, Wiley VCH.)

structures can be formed by spin-coating from chlorobenzene (CB)[198] and chloroform, respectively.[194] It has been reported that a homogeneous film is favored by slow evaporation and weak polymer–PCBM interaction, while rapid solvent evaporation and strong polymer–PCBM interaction leads to a lateral film structure. Interestingly, the multilayer structure shows the best performance of 3.5% PCE, with a higher J_{SC} and FF (Fig. 14D), despite excess hole-transporting material (APFO-3) accumulating at the cathode. The improved performance can be attributed to this functional structure that can favorably absorb photons and dissociate excitons at distinct regions, as well as the beneficial effect of PCBM content on charge mobilities compared to a homogeneous blend.[199–201] Efficient electron transport through a polymer-rich "skin" layer has been reported in MDMO-PPV:PCBM blends.[202] This result indicates that further investigation is required to correlate the engineering of the vertical morphology to the resulting device performance. Specific interactions of the blend component with the substrate, such as the interaction between the thiophene groups and gold, might pose an additional factor on the vertical morphology, especially in the vicinity of the substrate.[203]

3.3 Vertical phase separation in P3HT:PCBM

Vertical phase separation in the P3HT:PCBM system has been reported by several groups through various analysis techniques. Though the precise vertical composition profile is still under debate, the experimental results are discussed here for comparison. Kim *et al.* attributed the opposite device performance trend, particularly J_{SC}, upon annealing from different solvents to the distinct morphology distribution.[143] The higher boiling point of dichlorobenzene (DCB) allows more time for P3HT to segregate toward the PEDOT:PSS layer, while the faster evaporation of CB results in a more homogeneous composition. Campoy-Quiles *et al.* used variable-angle spectroscopic ellipsometry (VASE) to model the vertical composition profile of P3HT:PCBM thin films, and observed a common vertically and laterally phase-separated morphology under various preparation methods (Fig. 15).[34] A concentration gradient varying from PCBM-rich near the substrate to P3HT-rich adjacent to the surface was observed on both fused silica and PEDOT:PSS-coated substrates. The vertical composition profile retained a similar gradient after post-treatments, such as thermal and vapor annealing. Substrate treatment also substantially affected the vertical phase morphology. PEDOT:PSS resulted in a slightly less negative concentration gradient, while a hydrophobic hexamethyldisilazane SAM altered the vertical segregation, with P3HT accumulating at the substrate, and PCBM enriched at the air surface. It was inferred that the morphology evolution initialized from crystallization of the P3HT chains, followed by diffusion and segregation of the PCBM molecules.

Recently, the mixture solvent systems have been intensively explored by several groups, bringing a rather clear understanding of solvent-selection rules for desirable morphology.[3,5,204–206] We have investigated the role of alkanedithiols in the solvent mixtures for the P3HT:PCBM system. 1,8-Octanedithiol (OT) addition was found to preserve the P3HT crystallinity and redistribute the P3HT and PCBM phases in the blend film. XPS

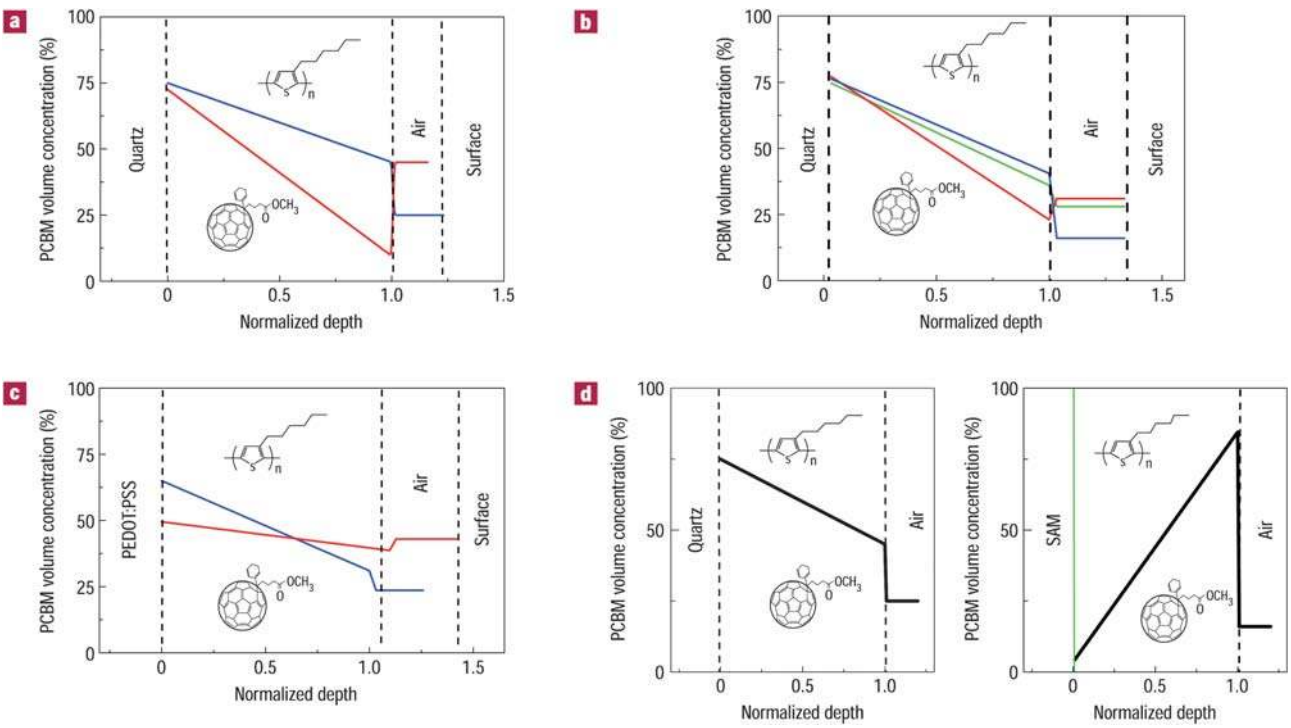

Fig. 15 Analysis of the ellipsometric data of the vertical PCBM concentration profiles in P3HT:PCBM films prepared under various conditions: (a) spin-coated on fused silica before (blue) and after (red) thermal annealing; (b) spin-coated on fused silica for 60 s at 5000 r.p.m. (blue), 3000 r.p.m. (green) and 700 r.p.m. (red); (c) spin-coated on PEDOT:PSS-coated fused silica before (blue) and after (red) vapor annealing; (d) spin-coated on fused silica (left) and on a Si wafer (with native oxide) precoated with a hydrophobic hexamethyldisilazane SAM. (Reprinted with permission from ref. 34; copyright 2008, Nature Publishing Group.)

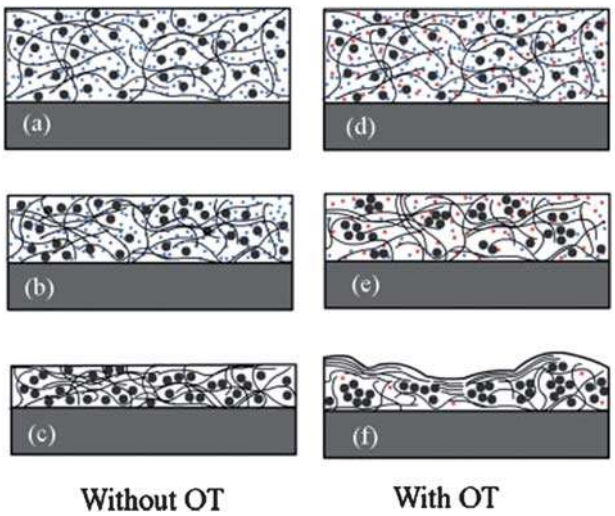

Fig. 16 Proposed model of film evolution during the spin-coating process. Black wire: P3HT polymer chain; large black dots: PCBM; blue dots: DCB molecules; and red dots: OT molecules. (a–c) correspond to three stages in the spin-coating process when DCB is the sole solvent; (d–f) correspond to three stages in the spin-coating process when OT is added to the DCB. Note the difference of PCBM distribution in the final stage of each case, (c) and (f). (Reprinted with permission from ref. 206; copyright 2008, Wiley-VCH.)

analysis revealed an inhomogeneous distribution (vertical phase separation) upon OT addition, where the polymer blend/PEDOT:PSS interface was enriched with PCBM. A model illustrating the effect of OT incorporation during the spin-coating process was proposed and illustrated in Fig. 16. The host solvent (DCB) has a lower boiling point (198 °C) than OT (270 °C), but a higher solubility for PCBM. As a result, the OT concentration gradually increased during the spin-coating process, with PCBM forming clusters and aggregates in the OT phase simultaneously. It has also been demonstrated that additive incorporation can alter the phase separation process for inverted BHJ cells.[207]

The buried interface was further investigated by lifting-off the polymer films from the substrate by immersion in water.[28] By attaching a fluorine atom on the phenyl ring of the PCBM molecule (FPCBM) provides a label to mark the PCBM distribution, as well as excluding possible effects of surface contaminants from oxygen and carbon. Furthermore, FPCBM allows the study of the polymer/PEDOT:PSS interface, which has long been hindered from elemental analysis due to the inevitable PEDOT:PSS remnant. It was shown that PCBM segregated at the substrate for both PEDOT:PSS and Cs_2CO_3-coated substrates. This vertical composition profile implies the intrinsic advantage of the inverted configuration, since the Cs_2CO_3 side (cathode) is PCBM-rich, and the Al (anode) side is P3HT-rich (Fig. 17), which should facilitate charge collection at the electrodes.[26,87] Rinsing the polymer blend film surface with OT selectively dissolves the PCBM to expose the top and bottom surface topography, as shown in Fig. 18.[205] The larger contrast in the phase image indicates the abundant fullerene phase of the bottom interface compared to the top surface (Fig. 18b). The vertical phase separation in the P3HT:PCBM blend film is ascribed to the lower surface energy of P3HT (γ_{P3HT}: 27 mN/m^2,

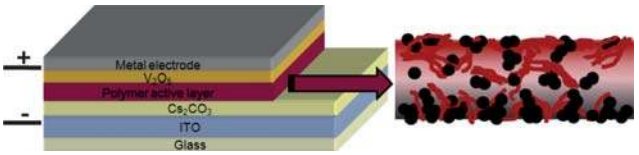

Fig. 17 Schematic of the inverted configuration and the vertical phase separation of the P3HT:PCBM blend. The red stripes and black dots represent the P3HT polymer chains and PCBM, respectively. (Reprinted with permission from ref. 28; copyright 2009, Wiley-VCH.)

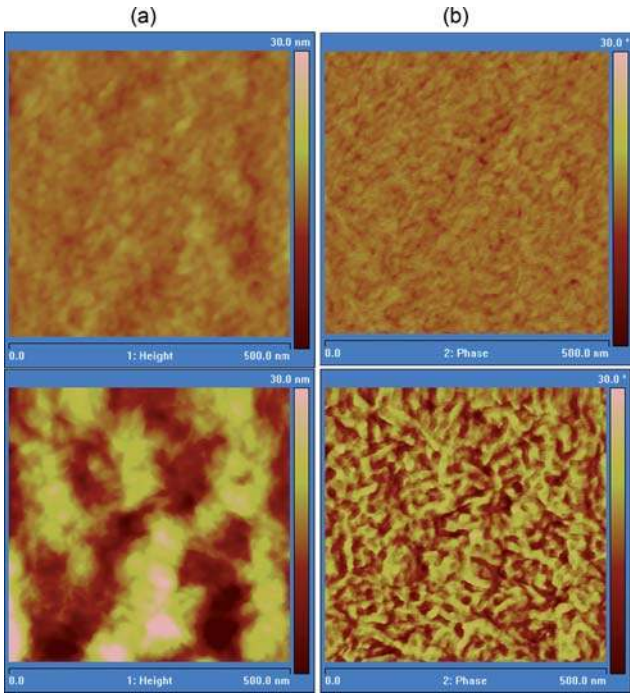

Fig. 18 AFM topography (left) and phase (right) images of (a) top and (b) bottom surfaces of the exposed P3HT networks. The PCBM was selectively removed using OT. (Reprinted with permission from ref. 28; copyright 2009, Wiley-VCH.)

γ_{PCBM}: 38 mN/m^2), and can be manipulated by varying the surface property/energy. The most significant PCBM accumulation occurring at the Cs_2CO_3-coated substrate is due to the strong charge transfer interaction between PCBM and the surface dipoles formed by Cs_2CO_3-coated ITO.[152,208]

Near-edge X-ray absorption fine structure spectroscopy (NEXAFS) is also capable of probing the buried interface composition in polymer solar cells.[209,210] NEXAFS also showed P3HT enrichment at the film surface despite the substrate treatment, whereas the amount of P3HT at the buried interface can be varied from 18% (on SiO_2) to 74% (on octyltrichlorosilane (OTS)) depending on the substrate surface energy. Despite the hydrophobic SAMs could form a P3HT-enriched contact at the substrate interface, the insulating nature of the SAMs impedes the hole collection, preventing the fabrication of high performance photovoltaic cells with preferred vertical composition profile *via* this approach. Indeed, this vertical composition gradient would impose a charge injection barrier at the electrodes. Hole-transport layers with lower surface energy,

electron-transport layers with higher surface energy, as well as the inverted configuration are expected to improve the device performance.[28,29,111] By using another depth-profiling technique, namely high kinetic energy XPS, different probing depths were achieved by varying the photon energies, which revealed a PCBM-enriched layer lying 6–20 nm under a polyfluorene-enriched surface layer by tracing the characteristic satellite features of the C_{60} cage.[211]

Transmission electron microscopy (TEM), X-ray diffraction (XRD) and scattering at both narrow and wide angles have been used to study the crystalline BHJ solar cells, particularly in the P3HT:PCBM system.[212–217] Scanning electron microscopy (SEM)[218,219] and atomic force microscopy (AFM) are commonly applied to probe the surface as well. However, these techniques only provide either localized or averaged information instead of a comprehensive view of the 3D nanoscale morphology. Recently, electron tomography has emerged as a powerful tool to characterize the 3D morphology of polymer solar cells.[220] The principle is illustrated in Fig. 19c, which lies in reconstructing the 3D nanoscale morphology in TEM by taking a series of 2D projections from different angles and tilting the sample specimen with respect to the electron beam. van Bavel *et al.* were the first to study polymer solar cells with electron tomography to reveal the 3D nanoscale organization, where slices close to the bottom and top of the film are shown in Fig. 19(a) and (b), respectively.[215] Electron diffraction showed low P3HT crystallinity with small crystals for as-cast film, while annealing treatment reorganizes the film morphology to form long P3HT nanorods. However, amorphous P3HT does not provide sufficient contrast to be differentiated from PCBM. An opposite vertical phase morphology compared to other analysis techniques was observed, with enrichment of P3HT nanorods near the anode and PCBM near the cathode for film thicknesses of 50 and 100 nm, as shown in Fig. 19(d).[221] P3HT aggregates existing in the solution might sediment due to gravity, forming nucleation sites for the P3HT nanorod enrichment. Andersson *et al.*[222] also utilized electron tomography to study the 3D nanomorphology of the APFO-3:PCBM blend system. It has been recently suggested that different types of vertical composition gradients could result from the varying film formation kinetics of different film thickness.[221] In summary, complementary techniques and further understanding of the phase separation kinetics are still required to elucidate the relationship between the vertical phase separation and device performance.

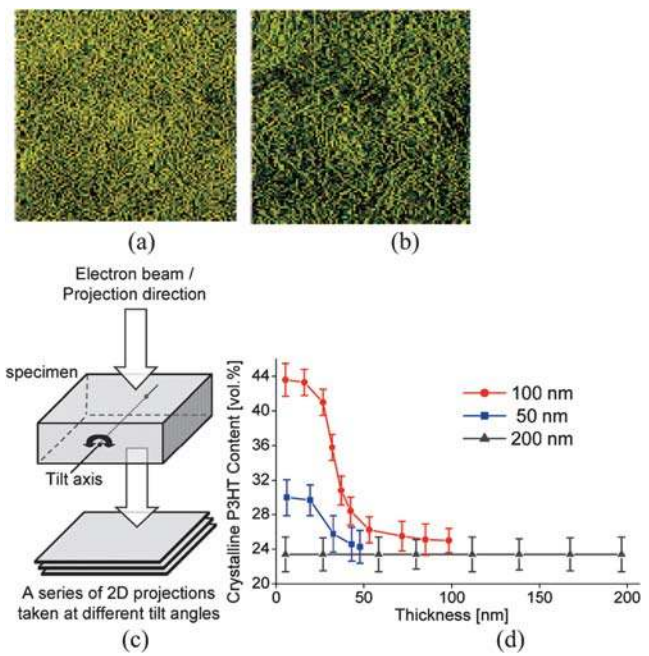

Fig. 19 Results of electron tomography: quantification of the crystalline P3HT nanorods distribution through the thickness of a thermally annealed P3HT:PCBM blend film (200 nm). Images (a) and (b) are slices taken out of the reconstructed volume of the film, with a slice (dimensions: 1700 nm × 1700 nm) located (a) close to the bottom of the film and (b) close to the top of the film. The crystalline P3HT nanorods are yellow in color. (c) The principle of electron tomography to reconstruct the 3D image of the specimen. (d) The relative area occupied by P3HT (yellow) in each slice (a, b) can thus be determined for all slices through the whole thickness of the P3HT:PCBM film. (Parts (a, b) reprinted with permission from ref. 215, part (c) from ref. 220 and part (d) from ref. 221; copyright 2009, American Chemical Society, and Royal Society of Chemistry.)

3.4 Utilization of the vertical phase separation

Despite the discrepancy of the vertical composition profile from electron tomography and other techniques, a composition gradient with the anode and cathode enriched with the donor and acceptor material, respectively, is evidently beneficial for the overall device performance. Significant efforts to realize the ideal vertical morphology in polymer solar cells have emerged, and some representative examples will be discussed in the following. In essence, three main approaches were employed to induce the favorable vertical phase morphology. Altering the vertical-stratified morphology by the solvent viscosity and substrate surface property have been demonstrated by several groups. Another approach is to incorporate species into the polymer blend solution to promote the formation of a preferred electrode contact. Different fabrication processes that are independent of the phase separation process of polymer blends have also been adapted to form a bilayer or p–i–n-like morphology.

Arias *et al.* altered the vertical phase separation in the poly-(9,9-dioctylfluorene-*co*-bis-*N*,*N*-(4-butylphenyl)-bis-*N*,*N*-phenyl-1,4-phenylenediamine) (PFB) and F8BT blend by either controlling the solvent-evaporation rate (solvent viscosity) or modifying the substrate surface properties.[177] Compared to using xylene as the solvent, a more viscous isodurene forms a vertical structure instead of lateral domains. Alternatively, using 7-OTS SAMs also formed a favorable segregation of the high-surface-energy component in the polymer blend. Fig. 20 confirmed the vertical phase separation by the observed filter effect *via* illumination from opposite sides of the device, where the layer adjacent to the transparent electrode partially filters the incident light.[223] The asymmetric absorption due to vertical segregation resulted in a different EQE with light illuminating from different sides, where the isodurene-cast films showed a much lower EQE when illuminated from the semitransparent Al cathode. Discussions of other organic electronic applications based on the vertically-segregated polymer blends was also reported by Arias.[224] Chen *et al.* used SAM microcontact printing (μCP) to pattern 3-aminopropyltriethoxysilane (APTES) SAMs on PEDOT:PSS

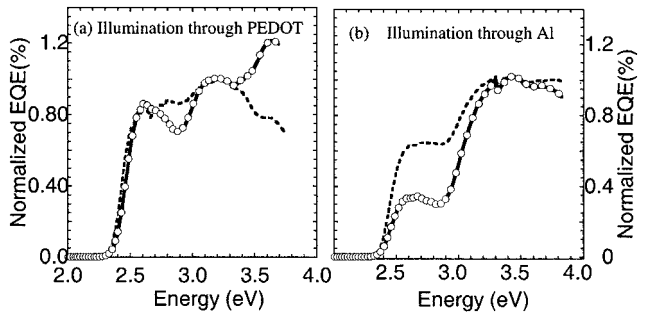

Fig. 20 Normalized EQE spectra of PFB:F8BT photovoltaic devices in which the active layer is composed either by PFB:F8BT blends with lateral phase separation (**---**) or with phase separation in the vertical direction (–○–). (a) Illumination through the PEDOT electrode and (b) through a semitransparent Al electrode. (Reprinted with permission from ref. 224; copyright 1997, The American Physical Society.)

to induce vertical segregation.[225] Surface-directed phase separation was obtained with a more complete phase separation. Absorption data confirmed improved P3HT alignment accompanied with a higher hole mobility.

Wei *et al.* incorporated a new fullerene derivative with a fluorocarbon chain (F-PCBM) into the P3HT:PCBM solution.[226] F-PCBM preferentially segregates a 2 nm thick layer at the surface due to the lower surface energy fluorinated side groups.[227] The high FF of 72% was attributed to the surface dipole moment induced by the F-PCBM layer, which decreased the energy barrier between the Al cathode and the PCBM. This also resembles an ideal vertical phase morphology, with the acceptor material enriched at the cathode to suppress charge recombination with the donor material. Similarly, surface-segregation of poly(dimethylsiloxane)-block-poly(methyl methacrylate) (PDMS-b-PMMA) formed by self-organization during spin-coating was demonstrated as an interfacial buffer layer.[228] A nanoscale functional interlayer of poly(ethylene glycol) (PEG) can also be formed *via* vertical phase separation to modify the film surface, which reacts with Al to reduce both the interfacial barrier height and contact resistance, as well as improve the device stability.[229]

Several other approaches have been employed to form a bilayer device structure with interpenetrating network, such as lamination,[230–232] interdiffusion,[233–236] and selective dissolution.[237] Wang *et al.* fabricated a bilayer device, where an intermixed zone with a concentration gradient was formed by spin-coating from separate solvents, namely P3HT in CB and PCBM in dichloromethane.[238] Shakutsui *et al.* controlled the distribution of the donor and acceptor materials by evaporative spray deposition using ultradilute solution (ESDUS) to form P3HT-rich/PCBM-rich BHJ solar cells.[239] The improved device performance was attributed to improved charge harvesting. Castro *et al.* utilized the surface-directed demixing concept on the immiscible poly[2-methoxy-5-(2′-ethylhexyloxy)-1,4-phenylene vinylene] (MEH-PPV)/PS (blend system, where the guest polymer (PS) was subsequently selectively removed. An efficient donor–acceptor heterojunction was formed by spin-coating or thermal evaporating a C_{60} layer, with a 3-fold improvement in PCE.[240]

We intentionally thermally-evaporated a thin layer of PCBM on top of the P3HT:PCBM blend film to modulate the vertical composition gradient, which resembles the p–i–n structure in inorganic and small molecule solar cells.[241] Upon thermal annealing, PCBM diffusion into the BHJ smoothens the top surface to increase the effective contact area as well as enrich the cathode interface with PCBM. The improved charge transport and extraction is reflected in the improved EQE over the entire absorption region. Vertical phase segregation was also observed in hybrid photovoltaics based on CdSe tetrapods and OC_1C_{10}-PPV blends by Sun *et al.*[242] It was shown that by replacing chloroform with a higher-boiling-point solvent, 1,2,4-trichlorobenzene (TCB), vertical segregation led to an improvement in charge-collection efficiency. Charge collection was more efficient even with a less efficient charge-dissociation rate due to the coarser phase separation, evidenced by the time-resolved photoluminescence (PL) measurement.

It is clear that vertical stratifications can be ascribed to the different solubilities and surface energies of the blend components as well as the dynamics of the spin-coating process. A volatile solvent is likely to form a more homogeneous film, while a less volatile solvent allows vertical phase separation. Upon vertical phase separation, the low surface energy component preferentially segregates at the surface or interface to reduce the overall energy. By controlling the film drying rate *via* solvent viscosity and spin-coating conditions as well as surface treatment, a closer to optimal, both laterally- and vertically-segregated morphology can be formed. If the vertical composition profile can be manipulated to the desired gradient, with a donor-enriched anode and acceptor-enriched cathode, efficient charge dissociation *via* the interpenetrating network as well as efficient charge transport along the interconnected pathway can be expected to vastly enhance the device performance.

4. Energy level alignment

One of the key issues for organic electronics is to understand the energy-level alignment at the interfaces. The interface electronic properties involving semiconducting and/or conducting molecules and polymers have been extensively investigated over the last two decades. A comprehensive review regarding the fundamental concepts of energy-level alignment at the organic/metal and organic/organic interfaces can be found by Ishii *et al.*[44] Two other excellent articles by Hwang *et al.* and Braun *et al.* have also reviewed the updated progress in this field.[243,244] Therefore, we will focus our emphasis on the recent work related to polymer photovoltaic devices.

Two different models have been proposed to describe the interfaces of the organic semiconductor and the metal/conductive substrate. When the organic molecule comes into contact with the clean metal surface, the electron wave function of the metal tails into the molecule in close proximity and broadens its energy level. As a result, an induced density of interface states (IDIS) is formed in the former energy gap of the organic molecules. In the IDIS model, the charge neutrality level (E_{CNL}) is calculated by integrating the local density of states in the IDIS and imposing the total number of electrons up to E_{CNL}, that equals the number of electrons in the neutral molecule. The relative position of the metal E_F and the organic E_{CNL}

determines the charge redistribution across the metal/organic interface. The charge transfer forms an interfacial dipole that narrows the energy difference between E_F and E_{CNL}. However, the actual charge injection barrier also depends on the density of states around E_{CNL} and can be described by the following two equations:

$$\phi_{Bn} = S(\phi_{sub} - EA) + (1 - S)E_{CNL} \quad (1)$$

$$S = \frac{1}{1 + 4\pi e^2 D_{is}\delta} \quad (2)$$

where ϕ_{Bn} is the electron injection barrier, ϕ_{sub} is the work function of the conductive substrate, EA is the electron affinity of the organic semiconductor (energy difference between vacuum and LUMO), D_{is} is the density of interface gap states, and δ is the effective metal–semiconductor distance.[243]

In contrast to organic small molecules deposited on the clean metal surface in high vacuum systems, polymer films are coated from solution to a substrate surface that is often contaminated with hydrocarbons and/or native oxides. The contamination layer physically and electronically decouples the polymer film from the continuum of the metallic electronic states.[245] Consequently, vacuum level alignment (Schottky–Mott limit) holds at the polymer/conductive substrate interface and the electron injection barrier equals the difference between the substrate E_F and EA of the polymer ($S = 1$).

In some cases, vacuum level shift is observed after polymer coating on the conductive substrate, which can be explained using the integer charge transfer (ICT) model. Although the contamination layer decouples the polymer layer from the substrate, charge transfer can still occur *via* tunneling as long as the contamination layer is sufficiently thin. Since the organic small molecules and conjugated polymers are soft materials, adding or withdrawing charges induces substantial electronic and geometric relaxation effects, leading to self-localized polaronic (single charge) or bipolaronic (double charge) states. These states are located in the previously forbidden band gap of the neutral molecule/polymer. The energy of the positive integer charge transfer state, E_{ICT+}, is defined as the energy required to take away one electron from the organic molecule or polymer, resulting in a fully relaxed state. The energy of the negative integer transfer state, E_{ICT-}, is defined as the energy gained by adding one electron to the organic molecule or polymer to produce a fully relaxed state. According to the ICT model, the energy level alignment of an organic/conductive substrate system with very weak interfacial interaction can be determined by the work function of the substrate (Φ_{SUB}) and the energy of the charge transfer states of the organic material. If Φ_{SUB} is larger than E_{ICT+} (Fig. 21a), electrons spontaneously flow from the organic layer to the substrate, creating an interfacial dipole that down-shifts the vacuum level. This process continues until the interface dipole equals $\Phi_{SUB} - E_{ICT+}$ and the Fermi level is pinned to the E_{ICT+} state at the interface. Consequently, in this condition the $\Phi_{ORG/SUB}$ remains invariant while the interface dipole changes with Φ_{SUB}. When Φ_{SUB} lies between the E_{ICT+} and the E_{ICT-} (Fig. 21b), no spontaneous charge transfer occurs at the substrate–organic interface. Therefore, vacuum level alignment holds and the work function of the substrate coated with organic layer $\Phi_{ORG/SUB}$ equals Φ_{SUB}. In the equilibrium

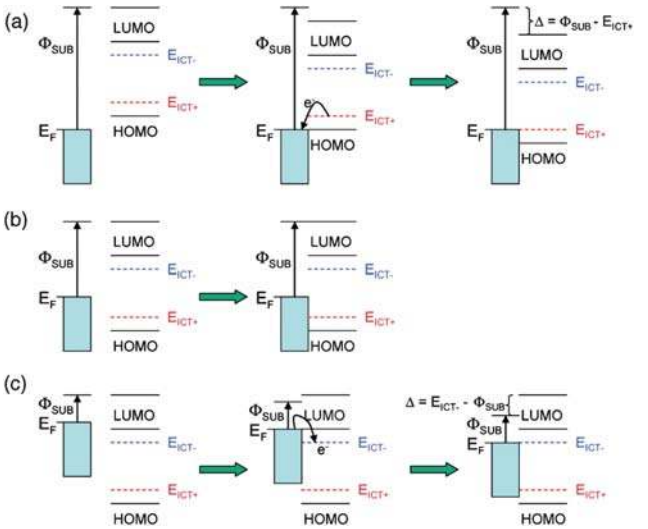

Fig. 21 Schematic illustration of the evolution of the energy-level alignment when a π-conjugated organic molecule or polymer is physisorbed on a substrate surface when (a) $\Phi_{SUB} > E_{ICT+}$: Fermi-level pinning to a positive integer charge-transfer state, (b) $E_{ICT-} < \Phi_{SUB} < E_{ICT+}$: vacuum level alignment, and (c) $\Phi_{SUB} < E_{ICT-}$: Fermi-level pinning to a negative integer charge-transfer state. The charge-transfer-induced shift in vacuum level, Δ, is shown where applicable. (Reprinted with permission from ref. 244; copyright 2009, Wiley VCH.)

case where Φ_{SUB} is smaller than E_{ICT-} (Fig. 21c), an interface dipole equal to $E_{ICT-} - \Phi_{SUB}$ is formed and the Fermi level is pinned to the CT^- state at the interface. The $\Phi_{ORG/SUB}$ in this case is also independent of Φ_{SUB}. Thus if the work function of the conductive substrates spans a sufficiently large range, a dependence between Φ_{SUB} and the work function of the organic-on-substrate interface $\Phi_{ORG/SUB}$ with sharp transitions between the vacuum alignment (Schottky–Mott limit, $E_{ICT-} < \Phi_{SUB} < E_{ICT+}$ with $\Phi_{ORG/SUB} = \Phi_{SUB}$) and Fermi level pinning ($\Phi_{SUB} < E_{ICT-}$ or $\Phi_{SUB} > E_{ICT+}$ with constant $\Phi_{ORG/SUB}$) regimes are expected, as shown in Fig. 22. However, in many experiments due to the limitation of Φ_{SUB}, only part of this region can be observed.

By using ultraviolet photoelectron spectroscopy (UPS), Tengstedt *et al.* mapped out the energy level alignment of 4 conjugated polymers on various conductive substrates with the

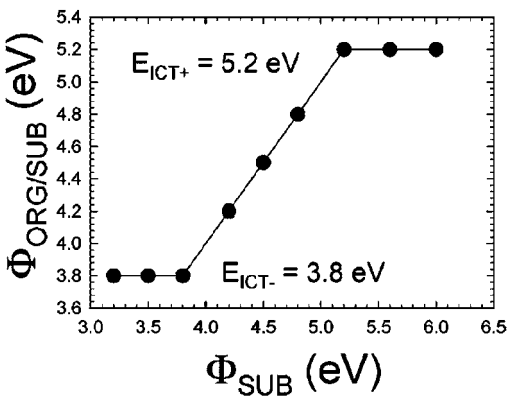

Fig. 22 General $\Phi_{ORG/SUB}$ *vs.* Φ_{SUB} dependence predicted by the ICT model. (Reprinted with permission from ref. 244; copyright 2009, Wiley VCH.)

Φ_{SUB} ranging from 3.8 to 6.1 eV.[246] The polymers tested were P3HT, TFB, poly(9-(1-decylundecylidene)fluorine) (P10AF), and poly(9,9-dioctylfluorene) (PFO), which reflect a large span in ionization potentials (IPs) (Table 2). Fig. 23 shows the dependence of $\Phi_{ORG/SUB}$ on Φ_{SUB} for the four polymers. When Φ_{SUB} is low, the $\Phi_{ORG/SUB}$ values of all the polymers equal Φ_{SUB} (slope = 1), indicating vacuum level alignment at the interface. For Φ_{SUB} exceeding a certain threshold value, the $\Phi_{ORG/SUB}$ becomes substrate-independent (slope = 0), implying that the Fermi level of the substrate is pinned to E_{ICT+}. Different materials have different thresholds. The threshold value for P3HT is 4.0 eV and thus the E_{ICT+} of P3HT can be determined as 4.0 eV, which is 0.5 eV above its HOMO. The E_{ICT+} values of all the 4 polymers are shown in Table 2. In a similar study, we determined the IP and E_{ICT+} to be 4.6 eV and 3.9 eV (Fig. 24).[247] Different energy alignment of P3HT with conductive substrates was also reported by others.[248] The difference may come from different P3HT morphology. For instance, Park *et al.* reported that depending on whether thermal treatment was used, the P3HT thin film adopts two different molecular orientations, parallel and perpendicular to the substrate, which result in different values of the vacuum level shift and hole-injection barrier.[249] Osikowicz *et al.* also reported that morphology change and interfacial doping may affect the E_{ICT+} level of P3HT and thus change the energy alignment between P3HT and the UV-ozone treated interface.[250]

The ICT model can also be used to understand the interface of small molecules on passivated conductive substrates. Using the above method, the E_{ICT+} of p-type small molecules can be determined.[251] Generally for acceptors coated on the conductive substrates, the Fermi level of the low work function substrate is pinned to the negative integer charge transfer state of these materials and vacuum level alignment is achieved when Φ_{SUB} exceeds certain threshold value (Fig. 25).[244] Thus the E_{ICT-} of these materials can be determined. The E_{ICT-} of C_{60} is 4.5 eV,[250] which is higher than that of PCBM shown in Fig. 24. The difference is consistent with Akaike *et al.*, that due to the side chain effect, the IE and EA of PCBM are 0.4–0.6 eV smaller than that of C_{60}.[252]

The organic/organic heterojunction interface in small molecule solar cells is also important because the energy offset between the donor and acceptor materials determines the charge separation process and the upper limit for the V_{OC}. A detailed introduction of the organic/organic interface of OLED and OPV devices can be found in a article by Armstrong *et al.*[253] Since only weak Van der Waals interaction exists at most organic/organic interfaces, the ICT model can also be used to understand the behavior of the organic/organic heterojunctions. Take the P3HT/C_{60} interface as an example: because the E_{ICT+} of P3HT (4.0 ± 0.1 eV) is smaller than the E_{ICT-} of C_{60} (4.5 ± 0.1 eV), electron transfer from P3HT to C_{60} is expected at the interface. As predicted by the ICT model, a potential of 0.5 ± 0.1 eV will build up at equilibrium to match the energy difference between the E_{ICT+} of P3HT and the E_{ICT-} of C_{60}. Osikowicz *et al.* studied the P3HT/C_{60} interface on aluminium (with native oxide layer), Al/Al_xO_y (Φ_{SUB} = 3.3–3.7 eV), and silicon (with native oxide layer), Si/SiO_x (Φ_{SUB} = 4.4–4.9 eV) substrates. The measured dipole of (0.6 ± 0.1 eV) at the P3HT/C_{60} interface is in good agreement with the ICP model.[250] The ICT model was also tested on the PFO/C_{60} and other organic/organic interfaces.[254,255] It was found that both the relative position between the charge transfer states of the materials forming the interface, and their energetic position with respect to the Fermi level of the substrate is important. For example, the E_{ICT+} of 4,4′-*N*,*N*′-dicarbazolylbiphenyl (CBP) and 4,4,4″-tris[3-methylphenyl(phenyl)amino]triphenylamine (m-MTDATA) are (5.2 ± 0.1 eV) and (4.5 ± 0.1 eV), respectively. When the CBP/m-MTDATA stack is deposited on the PEDOT:poly(perfluoroethylenesulfonic acid) (PFESA) substrate (Φ_{SUB} = 5.6–6.1 eV), the ICT model predicts the Fermi

Table 2 Estimates of essential parameters characterizing the energetics at the interface, as deduced from UPS measurements: IP, polaronic energy, and polaronic relaxation energy. (Reprinted with permission from ref. 246; copyright 2006, American Institute of Physics)

ELP	IP [± 0.1 eV]	Polaronic energy [± 0.05 V]	Relaxation energy [± 0.05 V]
P3HT	4.5	4.0	0.5
TFB	5.4	4.7	0.7
P10AF	5.5	5.1	0.4
PFO	5.8	5.2	0.6

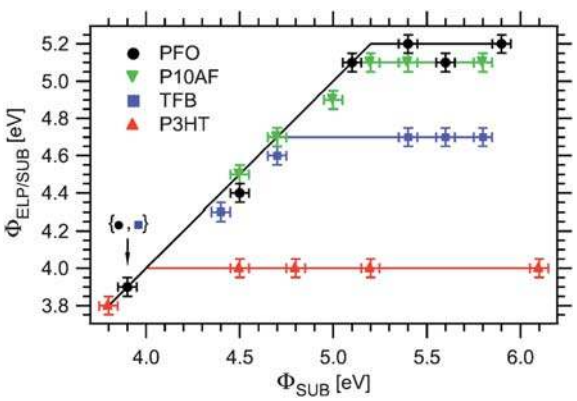

Fig. 23 Dependence of work function of polymer coated substrate, $\Phi_{ELP/SUB}$, on the work function of bare substrate, Φ_{SUB}, for four studied materials, namely P3HT, TFB, P10AF, and PFO. (Reprinted with permission from ref. 246; copyright 2006, American Institute of Physics.)

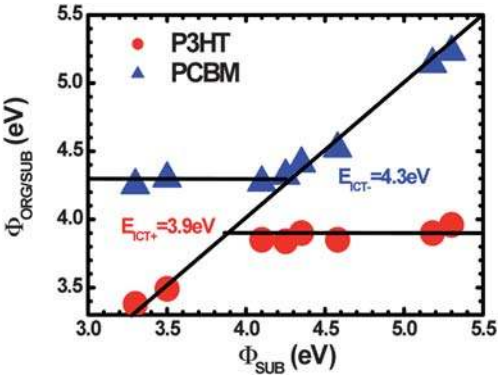

Fig. 24 Dependence of the work function of the substrate coated with organic semiconductor, $\Phi_{ORG/SUB}$, on the work function of bare substrate, Φ_{SUB}, for P3HT and PCBM. (Reprinted from ref. 247; copyright 2009, American Institute of Physics.)

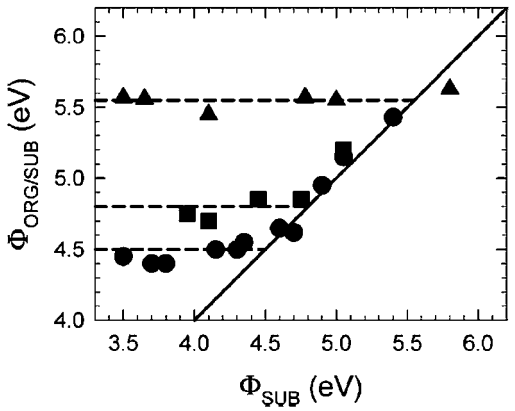

Fig. 25 Dependence of the work function of molecule-coated substrates, $\Phi_{ORG/SUB}$, on the work function of bare substrate, Φ_{SUB}, for C_{60} (●), TCNQ (■), and F4-TCNQ (▲). (Reprinted with permission from ref. 244; copyright 2009, Wiley VCH.)

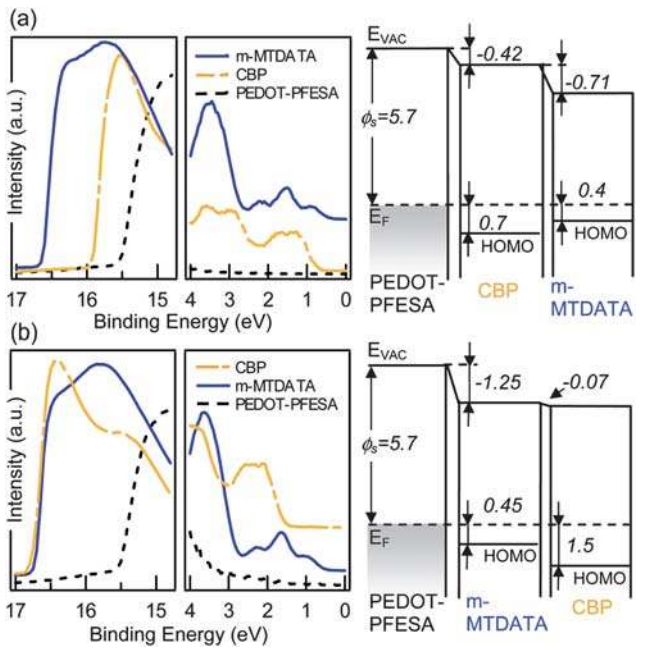

Fig. 26 UPS spectra and the corresponding diagrams of energy level alignment of interfaces: (a) PEDOT-PFESA/CBP/m-MTDATA; (b) Si/SiO_x/CBP/m-MTDATA. (Reprinted with permission from ref. 255; copyright 2009, American Institute of Physics.)

level alignment of the substrate with the E_{ICT+} of CBP and m-MTDATA, resulting a 0.7 eV dipole at the m-MTDATA on CBP interface, which lowers the vacuum level to 4.6 eV (Fig. 26a). In contrast, when a smaller work function silicon Si/$SiO_x$is used as the substructure, the ICT model predicts vacuum level alignment at both the substrate/CBP and CBP/m-MTDATA interfaces (Fig. 26b). The experimental results correspond well with the ICT model predictions.[255]

From the ICT model, knowing the substrate work function and the ICT states in organic materials constituting a multilayered structure should enable the prediction of the energy level alignment across the organic film stack. However, flat bilayer interfaces do not exist in the blend systems and works revealing the electronic structures in BHJs are scarce.[247,256] We recently used UPS to investigate the energy level alignment of the P3HT:PCBM BHJ and showed that the ICT model can also be employed to explain the results.

The E_{ICT+} of P3HT and E_{ICT-} of PCBM were first determined using the above method. (Fig. 24) Accordingly, the energy level alignment between the P3HT (or PCBM) layer and the inert substrates can be predicted using the ICT model. The work function of PEDOT:PSS-coated ITO determined by UPS is 5.0 eV. Since this value is larger than the E_{ICT+} of P3HT and lies between the E_{ICT+} and E_{ICT-} of PCBM, Fermi level pinning and vacuum level alignment is expected at the PEDOT:PSS/P3HT and the PEDOT:PSS/PCBM interface, respectively. As a result, the $\Phi_{ORG/SUB}$ is anticipated to be 3.9 eV for PEDOT:PSS/P3HT (Fig. 27a) and 5.0 eV for PEDOT:PSS/PCBM (Fig. 27b), consistent with the results obtained from the secondary electron cutoffs shown in Fig. 27d. Moreover, energy alignment of PCBM/P3HT stack on PEDOT:PSS can also be predicted. Because the E_{ICT+} of P3HT is smaller than the E_{ICT-} of PCBM, electrons will flow from P3HT to PCBM until the E_{ICT+} state of P3HT aligns with the E_{ICT-} state of PCBM at the interface. As a result, an interface dipole of −0.4 eV forms and the vacuum level of the P3HT layer is 4.6 eV above the Fermi level ($\Phi_{ORG/SUB}$ = 4.6 eV) (Fig. 27). Fig. 27d shows the UPS spectra of different P3HT:PCBM blends spin-coated on PEDOT:PSS. From the HOMO structure (right) it can be found that the UPS signals of the blend films are dominated by the P3HT component, which is consistent with the vertical phase separation discussed previously. Moreover, the IPs calculated from the UPS spectra of the blend films are around 4.6 eV and in agreement with ref. 246 and 250. The energy level alignment of the P3HT at the top surfaces of the blend films can thus be acquired from the UPS spectra. The UPS spectra of the blend films with low PCBM concentration (5:1, 3:1) are almost identical with pristine P3HT. Therefore, the energy level alignment of P3HT at the top of the blend film is the same as on PEDOT:PSS (or on top of the PEDOT:PSS/PCBM/…/P3HT stack, as predicted by the ICT model). As the PCBM concentration increases, the UPS spectrum shifts to lower binding energy, indicating a higher work function and a shallower HOMO level. It should be noted that the energy levels obtained from the UPS spectrum of the 1:5 weight ratio blend film are almost the same as those of the P3HT layer shown in Fig. 27c. In addition, the ICT model also predicts the same results for the P3HT layer on top of the PEDOT:PSS/PCBM/P3HT/…/PCBM stack. These resemblances suggest that P3HT covers most of the bottom surface (PEDOT:PSS/blends interface) of the 5:1 blend film and PCBM dominates the equivalent region of the 1:5 blend film. The PCBM/P3HT wt ratio at the bottom surface of the 5:1 film is estimated to be about 0.25. This value is much lower than the corresponding ratio of the 1:1 film, where the ratio is estimated to be around 1.8. Campoy-Quiles *et al.* estimated that the PCBM concentration at the PEDOT:PSS side of the 1:1 blend film is about 65 vol%.[34] Based on these data, a full coverage of PCBM at the PEDOT:PSS side can be expected in the 1:5 blend film.

The P3HT:PCBM blend films on Cs_2CO_3-covered ITO were also investigated and confirmed the above finding. The work function of Cs_2CO_3-coated ITO substrates can range from 3.05 to 3.8 eV, depending on different Cs_2CO_3 solution

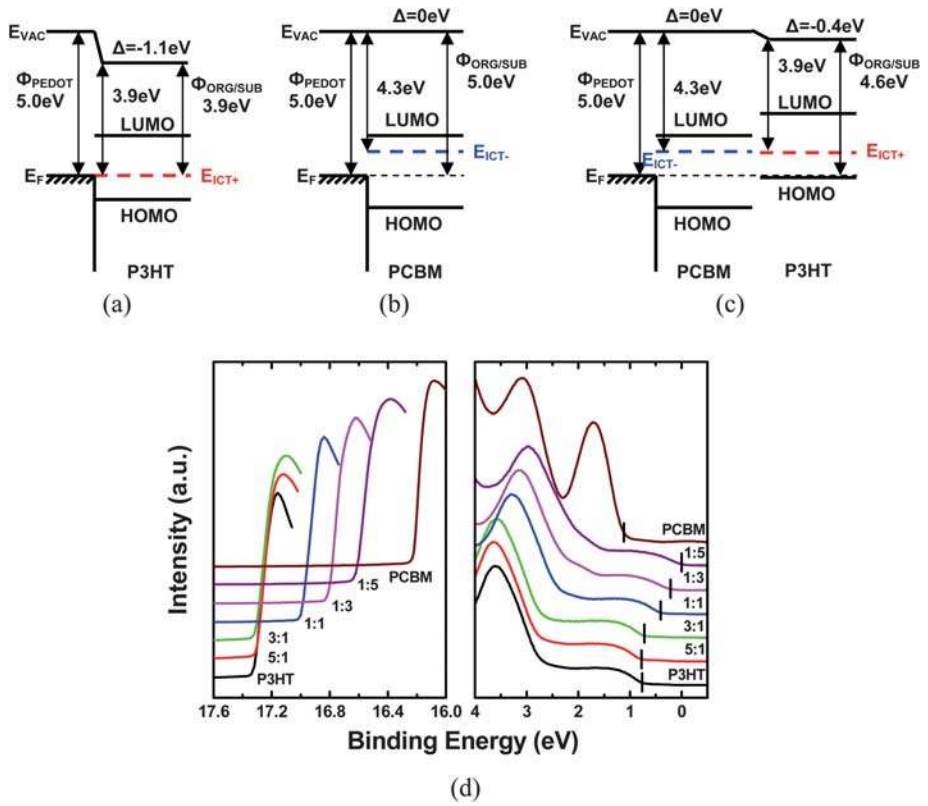

Fig. 27 Schematic energy level alignment diagrams of (a) PEDOT:PSS/P3HT, (b) PEDOT:PSS/PCBM, (c) PEDOT:PSS/PCBM/P3HT as predicted by the ICT model and (d) UPS spectra of P3HT, P3HT:PCBM, and PCBM films spin-coated on PEDOT:PSS. The PCBM concentration increases from bottom to top. (Reprinted with permission from ref. 247; copyright 2009, American Institute of Physics.)

concentrations and deposition processes used. In this case, the substrate work function is determined to be 3.5 eV, which is between the E_{ICT+} and E_{ICT-} of P3HT and smaller than the E_{CT-} of PCBM. Therefore, vacuum alignment was found at the Cs_2CO_3/P3HT interface ($\Phi_{ORG/SUB}$ = 3.5 eV) (Fig. 28a) and Fermi level pinning was found at the Cs_2CO_3/PCBM interface ($\Phi_{ORG/SUB}$ = 4.3 eV) (Fig. 28b). The UPS spectra of different P3HT:PCBM blend films also illustrate a P3HT-rich region near the top surface. However, unlike coated on PEDOT:PSS, even the film with the lowest PCBM concentration (5:1) shows obviously different energy levels from pristine P3HT when coated on Cs_2CO_3. As the P3HT concentration increases, the energy level alignment of the top P3HT of the blend approaches the energy level alignment of P3HT on Cs_2CO_3/P3HT predicted by the ICT model (Fig. 28c). The results are consistent with previous findings where PCBM tends to accumulate at the Cs_2CO_3 surface.[28] The P3HT/PCBM weight ratio at the bottom surface of the 5:1 film is about 2.0, which is close to the corresponding ratio (2.2) of the 1:1 film.

The interface between the organic layer and top electrode usually exhibits different energetic and charge carrier injection properties from its metal-on-organic counterpart. The atoms evaporated from a hot source often diffuse into the soft organic layer and induce significant damage. The metal atom can also react with the organic molecule/polymer and form chemical bonds, which causes local variations in both dipole energy and molecular-orbital modification, creating a distribution of injection barriers and trap energies at the electrode.[244] Thus the IDIS and ICT models can not be generally applied to these systems. Interfaces formed between P3HT and vapor-deposited Na, Cu, Ag, Au, Cr, V and Ti were reported.[257–259] With the exception of Au, interfacial chemical reactions were found between P3HT and all the other metals. Among them, Na, Cu and Ag react exclusively with the S atom, while Cr, V and Ti react with both the S and C atoms of the thiophene ring at higher coverages. Recently, it was found that when deposited onto the P3HT surface, Ca atoms react with defect sites or residual contamination.[260,261] At a low coverage region (between 0.1 to 0.6 monolayer (ML)), the Ca atoms cleave the C–S bonds in the thiophene group below the surface and form CaS clusters. It was revealed that Ca ultimately reacts with S atoms down to a depth of about 0.3 nm, which corresponds to 1.2×10^{15} atoms of reacted sulfur atoms per cm^2, or nearly five monomer-unit layers. The adsorbed Ca also forms 3D Ca clusters on the surface of the polymer at high coverages. This process predominates above 2 ML coverage and leads to the formation of a continuous Ca multilayer film beyond 11 ML coverage.[260] It was also found that after depositing 1 nm of Ca, the HOMO and LUMO of the P3HT down-shifted about 0.4 eV and the electron injection barrier was estimated to be about 0.98 eV.[261] However, this information has yet to provide a complete picture, since the energy level alignment between P3HT and Ca is not as critical as that of PCBM and Ca, where electron collection occurs in a typical device structure, and determines the overall performance of the P3HT:PCBM devices.

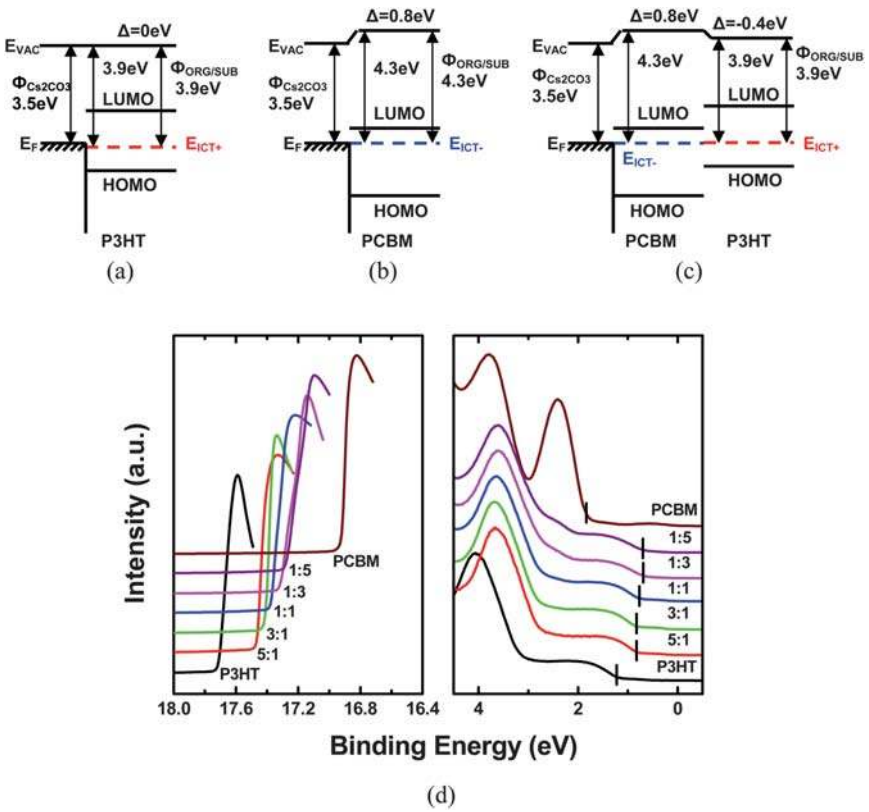

Fig. 28 Schematic energy level alignment diagrams of (a) Cs_2CO_3/P3HT, (b) Cs_2CO_3/PCBM, (c) Cs_2CO_3/PCBM/P3HT as predicted by the ICT model and (d) UPS spectra of P3HT, P3HT:PCBM, and PCBM films spin-coated on Cs_2CO_3. The PCBM concentration increases from bottom to top. (Reprinted with permission from ref. 247; copyright 2009, American Institute of Physics.)

Summary and outlook

The device performance of polymer solar cells depends on the sequential processes of charge dissociation, transport, and collection. The interfacial contact plays a central role in the charge collection and vertical phase separation process. A myriad of interfacial materials to engineer the anode and cathode contacts are highlighted. The vertical phase morphology is of fundamental importance to the charge-transport process, and charge recombination can be reduced *via* an optimized vertical composition gradient; that is, a donor-enriched anode and an acceptor-enriched cathode. However, high performance photovoltaic cells cannot be obtained with an inferior interface contact, and tremendous efforts are made to engineer the interface at the nanoscale. A better understanding and control of the interface properties of polymer solar cells shall allow us to derive a general design rule to engineer future material systems for polymer photovoltaic application.

With recent reports on significant advancement of donor materials, record PCEs have been pushed forward from *ca.* 5% to over 7% within the past few years, indicating promising potential for further efficiency improvement.[4,5] Though P3HT:PCBM BHJs with different morphologies have been intensively studied and well-understood with respect to electrode contact and morphological characteristics, it is a unique system which only provides limited information on the interface engineering for future improvement. Molecular engineering usually aims to achieve polymers with tunable HOMO levels and band gaps that ensure broad absorption and low potential loss. It requires different building blocks to construct copolymers which generally have lower crystallinity than P3HT. This lack of crystallinity leads to alower mobility and carrier diffusion length. Consequently, the film thicknesses and phase separation morphology are restricted in BHJ photovoltaic cells based on these copolymers, while commonly the amorphous films result in smaller carrier diffusion length and uniform distribution of donor and acceptor. It is thus more important to obtain highly selective and barrier-free charge collection *via* utilizing proper functional interlayers. Meanwhile, the surface effects on the polymer BHJ morphology should provide further possibility to manipulate the film evolution dynamics. Given efficient single BHJ photovoltaic cells with efficiencies approaching 10%, it is also desirable to stack BHJs with complementary absorption in tandem cells. The success in tandem structures also lies in superior interface materials and sufficient understanding of the interfacial contacts, which should help pave the route towards a double-digit efficiency.

References

1 G. Li, V. Shrotriya, J. Huang, Y. Yao, T. Moriarty, K. Emery and Y. Yang, *Nat. Mater.*, 2005, **4**, 864.
2 W. Ma, C. Yang, X. Gong, K. Lee and A. J. Heeger, *Adv. Funct. Mater.*, 2005, **15**, 1617.
3 J. Peet, J. Y. Kim, N. E. Coates, W. L. Ma, D. Moses, A. J. Heeger and G. C. Bazan, *Nat. Mater.*, 2007, **6**, 497.
4 S. H. Park, A. Roy, S. Beaupre, S. Cho, N. Coates, J. S. Moon, D. Moses, M. Leclerc, K. Lee and A. J. Heeger, *Nat. Photonics*, 2009, **3**, 297.

5 H.-Y. Chen, J. Hou, S. Zhang, Y. Liang, G. Yang, Y. Yang, L. Yu, Y. Wu and G. Li, *Nat. Photonics*, 2009, **3**, 649.
6 I. D. Parker, *J. Appl. Phys.*, 1994, **75**, 1656.
7 V. D. Mihailetchi, P. W. M. Blom, J. C. Hummelen and M. T. Rispens, *J. Appl. Phys.*, 2003, **94**, 6849.
8 J. Nelson, J. Kirkpatrick and P. Ravirajan, *Phys. Rev. B: Condens. Matter Mater. Phys.*, 2004, **69**, 035337.
9 B. P. Rand, D. P. Burk and S. R. Forrest, *Phys. Rev. B: Condens. Matter Mater. Phys.*, 2007, **75**, 115327.
10 T. Kirchartz, J. Mattheis and U. Rau, *Phys. Rev. B: Condens. Matter Mater. Phys.*, 2008, **78**, 235320.
11 J. J. Benson-Smith, L. Goris, K. Vandewal, K. Haenen, J. V. Manca, D. Vanderzande, D. D. C. Bradley and J. Nelson, *Adv. Funct. Mater.*, 2007, **17**, 451.
12 K. Vandewal, K. Tvingstedt, A. Gadisa, O. Inganäs and J. V. Manca, *Nat. Mater.*, 2009, **8**, 904.
13 M. A. Loi, S. Toffanin, M. Muccini, M. Forster, U. Scherf and M. Scharber, *Adv. Funct. Mater.*, 2007, **17**, 2111.
14 M. Hallermann, S. Haneder and E. D. Como, *Appl. Phys. Lett.*, 2008, **93**, 053307.
15 D. Veldman, Ö. İpek, S. C. J. Meskers, J. Sweelssen, M. M. Koetse, S. C. Veenstra, J. M. Kroon, S. S. van Bavel, J. Loos and R. A. J. Janssen, *J. Am. Chem. Soc.*, 2008, **130**, 7721.
16 K. Vandewal, A. Gadisa, W. D. Oosterbaan, S. Bertho, F. Banishoeib, I. V. Severen, L. Lutsen, T. J. Cleij, D. Vanderzande and J. V. Manca, *Adv. Funct. Mater.*, 2008, **18**, 2064.
17 Y. Hirose, A. Kahn, V. Aristov, P. Soukiassian, V. Bulovi and S. R. Forrest, *Phys. Rev. B: Condens. Matter*, 1996, **54**, 13748.
18 P. Peumans, V. Bulovic and S. R. Forrest, *Appl. Phys. Lett.*, 2000, **76**, 2650.
19 P. Peumans and S. R. Forrest, *Appl. Phys. Lett.*, 2001, **79**, 126.
20 M. Vogel, S. Doka, Ch. Breyer, M. Ch. Lux-Steiner and K. Fostiropoulos, *Appl. Phys. Lett.*, 2006, **89**, 163501.
21 C. Waldauf, M. Morana, P. Denk, P. Schilinsky, K. Coakley, S. A. Choulis and C. J. Brabec, *Appl. Phys. Lett.*, 2006, **89**, 233517.
22 A. Hayakawa, O. Yoshikawa, T. Fujieda, K. Uehara and S. Yoshikawa, *Appl. Phys. Lett.*, 2007, **90**, 163517.
23 M. D. Irwin, D. B. Buchholz, A. W. Hains, R. P. H. Chang and T. J. Marks, *Proc. Natl. Acad. Sci. U. S. A.*, 2008, **105**, 2783.
24 L. S. Hung and C. H. Chen, *Mater. Sci. Eng., R*, 2002, **39**, 143.
25 K. Walzer, B. Maennig, M. Pfeiffer and K. Leo, *Chem. Rev.*, 2007, **107**, 1233.
26 G. Li, C.-W. Chu, V. Shrotriya, J. Huang and Y. Yang, *Appl. Phys. Lett.*, 2006, **88**, 253503.
27 S. K. Hau, H.-L. Yip, N. S. Baek, J. Zou, K. O'Malley and A. K.-Y. Jen, *Appl. Phys. Lett.*, 2008, **92**, 253301.
28 Z. Xu, L.-M. Chen, G. W. Yang, C.-H. Huang, J. H. Hou, Y. Wu, G. Li, C.-S. Hsu and Y. Yang, *Adv. Funct. Mater.*, 2009, **19**, 1227.
29 L.-M. Chen, Z. Hong, G. Li and Y. Yang, *Adv. Mater.*, 2009, **21**, 1434.
30 R. A. L. Jones, L. J. Norton, E. J. Kramer, F. S. Bates and P. Wiltzius, *Phys. Rev. Lett.*, 1991, **66**, 1326.
31 G. Krausch, C. A. Dai, E. J. Kramer, J. Marko and F. S. Bates, *Macromolecules*, 1993, **26**, 5566.
32 S. Walheim, M. Böltau, J. Mlynek, G. Krausch and U. Steiner, *Macromolecules*, 1997, **30**, 4995.
33 S. Khodabakhsh, B. M. Sanderson, J. Nelson and T. S. Jones, *Adv. Funct. Mater.*, 2006, **16**, 95.
34 M. Campoy-Quiles, T. Ferenczi, T. Agostinelli, P. G. Etchegoin, Y. Kim, T. D. Anthopoulos, P. N. Stavrinou, D. D. C. Bradley and J. Nelson, *Nat. Mater.*, 2008, **7**, 158.
35 S. T. Lee, Z. Q. Gao and L. S. Hung, *Appl. Phys. Lett.*, 1999, **75**, 1404.
36 K. Suemori, M. Yokoyama and M. Hiramoto, *J. Appl. Phys.*, 2006, **99**, 036109.
37 C. Uhrich, R. Schueppel, A. Petrich, M. Pfeiffer, K. Leo, E. Brier, P. Kilickiran and P. Baeuerle, *Adv. Funct. Mater.*, 2007, **17**, 2991.
38 A. Kumar, S. Sista and Y. Yang, *J. Appl. Phys.*, 2009, **105**, 094512.
39 J. Y. Kim, S. H. Kim, H. H. Lee, K. H. Lee, W. L. Ma, X. Gong and A. J. Heeger, *Adv. Mater.*, 2006, **18**, 572.
40 A. Roy, S. H. Park, S. Cowan, M. H. Tong, S. Cho, K. Lee and A. J. Heeger, *Appl. Phys. Lett.*, 2009, **95**, 013302.
41 J. Gilot, I. Barbu, M. M. Wienk and R. A. J. Janssen, *Appl. Phys. Lett.*, 2007, **91**, 113520.
42 B. V. Andersson, D. M. Huang, A. J. Moulé and O. Inganäs, *Appl. Phys. Lett.*, 2009, **94**, 043302.
43 N. Uyeda, T. Kobayashi, K. Ishizuka and Y. Fujiyoshi, *Nature*, 1980, **285**, 95.
44 H. Ishii, K. Sugiyama, E. Ito and K. Seki, *Adv. Mater.*, 1999, **11**, 605.
45 Y. Hirose, A. Kahn, V. Arisotov and P. Soukiassian, *Appl. Phys. Lett.*, 1996, **68**, 217.
46 H. Oji, E. Ito, M. Furuta, K. Kajikawa, H. Ishii, Y. Ouchi and K. Seki, *J. Electron Spectrosc. Relat. Phenom.*, 1999, **101–103**, 517.
47 S. K. Hau, H.-L. Yip, K. Leong and A. K.-Y. Jen, *Org. Electron.*, 2009, **10**, 719.
48 J.-Y. Lee, S. T. Connor, Y. Cui and P. Peumans, *Nano Lett.*, 2008, **8**, 689.
49 M. Lögdlund and J. L. Brédas, *J. Chem. Phys.*, 1994, **101**, 4357.
50 H. Antoniadis, B. R. Hsieh, M. A. Abkowitz, S. A. Jenekhe and M. Stolka, *Synth. Met.*, 1994, **62**, 265.
51 G. Yu, C. Zhang and A. J. Heeger, *Appl. Phys. Lett.*, 1994, **64**, 1540.
52 G. Yu, K. Pakbaz and A. J. Heeger, *Appl. Phys. Lett.*, 1994, **64**, 3422.
53 C. J. Brabec, A. Cravino, D. Meissner, N. S. Sariciftci, T. Fromherz, M. T. Rispents, L. Sanchez and J. C. Hummelen, *Adv. Funct. Mater.*, 2001, **11**, 374.
54 D. Gupta, M. Bag and K. S. Narayan, *Appl. Phys. Lett.*, 2008, **92**, 093301.
55 J. M. Bharathan and Y. Yang, *J. Appl. Phys.*, 1998, **84**, 3207.
56 S. Cros, M. Firon, S. Lenfant, P. Trouslard and L. Beck, *Nucl. Instrum. Methods Phys. Res., Sect. B*, 2006, **251**, 257.
57 M. O. Reese, M. S. White, G. Rumbles, D. S. Ginley and S. E. Shaheen, *Appl. Phys. Lett.*, 2008, **92**, 053307.
58 L. S. Hung, C. W. Tang and M. G. Mason, *Appl. Phys. Lett.*, 1997, **70**, 152.
59 S. E. Shaheen, G. E. Jabbour, M. M. Morrell, Y. Kawabe, B. Kippelen, N. Peyghambarian, M.-F. Nabor, R. Schlaf, E. A. Mash and N. R. Armstrong, *J. Appl. Phys.*, 1998, **84**, 2324.
60 L. S. Hung, R. Q. Zhang, P. He and M. G. Mason, *J. Phys. D: Appl. Phys.*, 2002, **35**, 103.
61 G. E. Jabbour, B. Kippelen, N. R. Armstrong and N. Peyghambarian, *Appl. Phys. Lett.*, 1998, **73**, 1185.
62 T. Hasegawa, S. Miura, T. Moriyama, T. Kimura, I. Takaya, Y. Osato and H. Mizutani, in *SID Int. Symp. Digest Technol. Papers*, 2004, p. 154.
63 J. Huang, G. Li, E. Wu, Q. Xu and Y. Yang, *Adv. Mater.*, 2006, **18**, 114.
64 J. Huang, T. Watanabe, K. Ueno and Y. Yang, *Adv. Mater.*, 2007, **19**, 739.
65 Y. J. Yi, S. J. Kang, K. Cho, J. M. Koo, K. Han, K. J. Park, M. K. Noh, C. N. Whang and K. H. Jeong, *Appl. Phys. Lett.*, 2005, **86**, 213502.
66 Y. Kim, J.-G. Lee and S. Kim, *Adv. Mater.*, 1999, **11**, 1463.
67 X. T. Tao, H. Suzuki, T. Wada, S. Miyata and H. Sasabe, *J. Am. Chem. Soc.*, 1999, **121**, 9447.
68 C. Ganzorig, K. Suga and M. Fujihira, *Mater. Sci. Eng., B*, 2001, **85**, 140.
69 J. Lee, Y. Park, S. K. Lee, E.-J. Cho, D. Y. Kim, H. Y. Chu, H. Lee, L.-M. Do and T. Zyung, *Appl. Phys. Lett.*, 2002, **80**, 3123.
70 J. Lee, Y. Park, D. Y. Kim, H. Y. Chu, H. Lee and L.-M. Do, *Appl. Phys. Lett.*, 2003, **82**, 173.
71 S. E. Shaheen, C. J. Brabec, N. S. Sariciftci, F. Padinger, T. Fromherz and J. C. Hummelen, *Appl. Phys. Lett.*, 2001, **78**, 841.
72 C. J. Brabec, S. E. Shaheen, C. Winder, N. S. Sacriciftci and P. Denk, *Appl. Phys. Lett.*, 2002, **80**, 1288.
73 W. J. H. van Gennip, J. K. J. van Duren, P. C. Thune, R. A. J. Janssen and J. W. Niemantsverdriet, *J. Chem. Phys.*, 2002, **117**, 5031.
74 B. N. Limketkai and M. A. Baldo, *Phys. Rev. B: Condens. Matter Mater. Phys.*, 2005, **71**, 085207.
75 S. K. M. Jönsson, E. Carlegrim, F. Zhang, W. R. Salaneck and M. Fahlman, *Jpn. J. Appl. Phys.*, 2005, **44**, 3695.
76 C. H. Lee, *Synth. Met.*, 1997, **91**, 125.
77 Y. S. Lee, J.-H. Park, Y.-H. Kwak, Y.-J. Kim and J. S. Choi, *Mol. Cryst. Liq. Cryst.*, 2003, **405**, 89.
78 J. Lee, Y. Park, D. Y. Kim, H. Y. Chu, H. Lee and L. M. Do, *Appl. Phys. Lett.*, 2003, **82**, 173.
79 S. Okada, K. Okinaka, H. Iwawaki, M. Furugori, M. Hashimoto, T. Mukaide, J. Kamatani, S. Igawa, A. Tsuboyama, T. Takiguchi and K. Ueno, *Dalton Trans.*, 2005, 1583.

80 E. Ahlswede, J. Hanisch and M. Powalla, *Appl. Phys. Lett.*, 2007, **90**, 163504.
81 J. Huang, W. J. Hou, J. H. Li, G. Li and Y. Yang, *Appl. Phys. Lett.*, 2006, **89**, 133509.
82 J. Huang, Z. Xu and Y. Yang, *Adv. Funct. Mater.*, 2007, **17**, 1966.
83 T. R. Briere and A. H. Sommer, *J. Appl. Phys.*, 1977, **48**, 3547.
84 C.-I. Wu, C.-T. Lin, Y.-H. Chen, M.-H. Chen, Y.-J. Lu and C.-C. Wu, *Appl. Phys. Lett.*, 2006, **88**, 152104.
85 M.-H. Chen and C.-I. Wu, *J. Appl. Phys.*, 2008, **104**, 113713.
86 A. H. Sommer, *J. Appl. Phys.*, 1980, **51**, 1254.
87 H.-H. Liao, L.-M. Chen, Z. Xu, G. Li and Y. Yang, *Appl. Phys. Lett.*, 2008, **92**, 173303.
88 F.-C. Chen, J.-L. Wu, S. S. Yang, K.-H. Hsieh and W.-C. Chen, *J. Appl. Phys.*, 2008, **103**, 103721.
89 F.-C. Chen, J.-L. Wu, K.-H. Hsieh, W.-C. Chen and S.-W. Lee, *Org. Electron.*, 2008, **9**, 1132.
90 A. Fujishima and K. Honda, *Nature*, 1972, **238**, 37.
91 B. O'Regan and M. Grätzel, *Nature*, 1991, **353**, 737.
92 A. Fujishima, T. N. Rao and D. A. Tryk, *J. Photochem. Photobiol., C*, 2000, **1**, 1.
93 A. L. Linsebigler, G. Lu and J. J. T. Yates, *Chem. Rev.*, 1995, **95**, 735.
94 K. H. Lee, J. Y. Kim, S. H. Park, S. H. Kim, S. N. Cho and A. J. Heeger, *Adv. Mater.*, 2007, **19**, 2445.
95 J. K. Lee, N. E. Coates, S. Cho, N. S. Cho, D. Moses, G. C. Bazan, K. Lee and A. J. Heeger, *Appl. Phys. Lett.*, 2008, **92**, 243308.
96 J. C. Yu, J. Yu, W. Ho, Z. Jiang and L. Zhang, *Chem. Mater.*, 2002, **14**, 3808.
97 C. Burda, Y. Lou, X. Chen, A. C. S. Samia, J. Stout and J. L. Gole, *Nano Lett.*, 2003, **3**, 1049.
98 N. Sekine, C.-H. Chou, W. L. Kwan and Y. Yang, *Org. Electron.*, 2009, **10**, 1473.
99 M.-H. Park, J.-H. Li, A. Kumar, G. Li and Y. Yang, *Adv. Funct. Mater.*, 2009, **19**, 1241.
100 J. Y. Kim, K. H. Lee, N. E. Coates, D. Moses, T.-Q. Nguyen, M. Dante and A. J. Heeger, *Science*, 2007, **317**, 222.
101 J. H. Hou, H.-Y. Chen, S. Zhang, G. Li and Y. Yang, *J. Am. Chem. Soc.*, 2008, **130**, 16144.
102 S. Sista, M.-H. Park, Z. R. Hong, Y. Wu, J. H. Hou, W. L. Kwan, G. Li and Y. Yang, *Adv. Mater.*, 2010, **22**, 380, DOI: 10.1002/adma.200901624.
103 T. Kuwabara, H. Sugiyama, T. Yamaguchi and K. Takahashi, *Thin Solid Films*, 2009, **517**, 3766.
104 A. L. Roest, J. J. Kelly, D. Vanmaekelbergh and E. A. Meulenkamp, *Phys. Rev. Lett.*, 2002, **89**, 036801.
105 J. Gilot, M. M. Wienk and R. A. J. Janssen, *Appl. Phys. Lett.*, 2007, **90**, 143512.
106 W. J. E. Beek, M. M. Wienk, M. Kemerink, X. Yang and R. A. J. Janssen, *J. Phys. Chem. B*, 2005, **109**, 9505.
107 F. Verbakel, S. C. J. Meskers and R. A. J. Janssen, *Appl. Phys. Lett.*, 2006, **89**, 102103.
108 B. Maennig, J. Drechsel, D. Gebeyehu, P. Simon, F. Kozlowski, A. Werner, F. Li, S. Grundmann, S. Sonntag, M. Koch, K. Leo, M. Pfeiffer, H. Hoppe, D. Meissner, N. S. Sariciftci, I. Riedel, V. Dyakonov and J. Parisi, *Appl. Phys. A: Mater. Sci. Process.*, 2004, **79**, 1.
109 J. S. Kim, J. H. Park, J. H. Lee, J. Jo, D.-Y. Kim and K. Cho, *Appl. Phys. Lett.*, 2007, **91**, 112111.
110 S. Khodabakhsh, D. Poplavskyy, S. Heutz, J. Nelson, D. D. C. Bradley, H. Murata and T. S. Jones, *Adv. Funct. Mater.*, 2004, **14**, 1205.
111 S. K. Hau, H.-L. Yip, O. Acton, N. S. Baek, H. Ma and A. K.-Y. Jen, *J. Mater. Chem.*, 2008, **18**, 5113.
112 G. K. Mor, K. Shankar, M. Paulose, O. K. Varghese and C. A. Grimes, *Appl. Phys. Lett.*, 2007, **91**, 152111.
113 T. C. Monson, M. T. Lloyd, D. C. Olson, Y.-J. Lee and J. W. P. Hsu, *Adv. Mater.*, 2008, **20**, 4755.
114 J. Veres, S. Ogier, G. Lloyd and D. d. Leeuw, *Chem. Mater.*, 2004, **16**, 4543.
115 I.-W. Hwang, C. Soci, D. Moses, Z. Zhu, D. Waller, R. Gaudiana, C. J. Brabec and A. J. Heeger, *Adv. Mater.*, 2007, **19**, 2307.
116 H.-L. Yip, S. K. Hau, N. S. Baek and A. K.-Y. Jen, *Appl. Phys. Lett.*, 2008, **92**, 193313.
117 H.-L. Yip, S. K. Hau, N. S. Baek, H. Ma and A. K.-Y. Jen, *Adv. Mater.*, 2008, **20**, 2376.
118 F. Zhang, M. Ceder and O. Inganäs, *Adv. Mater.*, 2007, **19**, 1835.
119 X. H. Chen, J. X. Yang, J. Lu, K. K. Manga, K. P. Loh and F. R. Zhu, *Appl. Phys. Lett.*, 2009, **95**, 133305.
120 J. Luo, H. B. Wu, C. He, A. Y. Li, W. Yang and Y. Cao, *Appl. Phys. Lett.*, 2009, **95**, 043301.
121 Y. Zhao, Z. Y. Xie, C. J. Qin, Yao Qu, Y. H. Geng and L. X. Wang, *Sol. Energy Mater. Sol. Cells*, 2009, **93**, 604.
122 S.-I. Na, S.-H. Oh, S.-S. Kim and D.-Y. Kim, *Org. Electron.*, 2009, **10**, 496.
123 Y. Cao, G. Yu, C. Zhang, R. Menon and A. J. Heeger, *Synth. Met.*, 1997, **87**, 171.
124 Y.-F. Lim, S. Lee, D. J. Herman, M. T. Lloyd, J. E. Anthony and G. G. Malliaras, *Appl. Phys. Lett.*, 2008, **93**, 193301.
125 M. P. de Jong, L. J. van IJzendoorn and M. J. A. d. Voigt, *Appl. Phys. Lett.*, 2000, **77**, 2255.
126 Y. H. Kim, S.-H. Lee, J. Noh and S.-H. Han, *Thin Solid Films*, 2006, **510**, 305.
127 K. W. Wong, H. L. Yip, Y. Luo, K. Y. Wong, W. M. Lau, K. H. Low, H. F. Chow, Z. Q. Gao, W. L. Yeung and C. C. Chang, *Appl. Phys. Lett.*, 2002, **80**, 2788.
128 H. Yan, P. Lee, N. R. Armstrong, A. Graham, G. A. Evmenenko, P. Dutta and T. J. Marks, *J. Am. Chem. Soc.*, 2005, **127**, 3172.
129 V. Shrotriya, G. Li, Y. Yao, C. Chu and Y. Yang, *Appl. Phys. Lett.*, 2006, **88**, 073508.
130 D. Y. Kim, J. Subbiah, G. Sarasqueta, F. So, H. J. Ding, Irfan and Y. L. Gao, *Appl. Phys. Lett.*, 2009, **95**, 093304.
131 D. Y. Kim, G. Sarasqueta and F. So, *Sol. Energy Mater. Sol. Cells*, 2009, **93**, 1452.
132 D. W. Zhao, W. S. X, C. Y. Jiang, A. K. K. Kyaw, G. Q. Lo and D. L. Kwong, *Appl. Phys. Lett.*, 2008, **93**, 083305.
133 N. Li, B. E. Lassiter, R. R. Lunt, G. Wei and S. R. Forrest, *Appl. Phys. Lett.*, 2009, **94**, 023307.
134 S. Han, W. S. Shin, M. Seo, D. Gupta, S.-J. Moon and S. Yoo, *Org. Electron.*, 2009, **10**, 791.
135 M. Y. Chan, C. S. Lee, S. L. Lai, M. K. Fung, F. L. Wong, H. Y. Sun, K. M. Lau and S. T. Lee, *J. Appl. Phys.*, 2006, **100**, 094506.
136 M. Kröger, S. Hamwi, J. Meyer, T. Riedl, W. Kowalsky and A. Kahn, *Appl. Phys. Lett.*, 2009, **95**, 123301.
137 J. Cui, Q. Huang, J. C. G. Veinot, H. Yan, Q. Wang, G. R. Hutchison, A. G. Richter, G. Evmenenko, P. Dutta and T. J. Marks, *Langmuir*, 2002, **18**, 9958.
138 A. W. Hains and T. J. Marks, *Appl. Phys. Lett.*, 2008, **92**, 023504.
139 B. Kang, L. W. Tan and S. R. P. Silva, *Appl. Phys. Lett.*, 2008, **93**, 133302.
140 C.-Y. Li, T.-C. Wen and T.-F. Guo, *J. Mater. Chem.*, 2008, **18**, 4478.
141 M. S. White, D. C. Olson, S. E. Shaheen, N. Kopidakis and D. S. Ginley, *Appl. Phys. Lett.*, 2006, **89**, 143517.
142 M. Andersen, J. E. Carle, N. Cruys-Bagger, M. R. Lilliedal, M. A. Hammond, B. Winther-Jensen and F. C. Krebs, *Sol. Energy Mater. Sol. Cells*, 2007, **91**, 539.
143 Y. K. Kim, S. A. Choulis, J. Nelson, D. D. C. Bradley, S. Cook and J. R. Durrant, *Appl. Phys. Lett.*, 2005, **86**, 063502.
144 R. Steim, S. A. Choulis, P. Schilinsky and C. J. Brabec, *Appl. Phys. Lett.*, 2008, **92**, 093303.
145 T. Ameri, G. Dennler, C. Waldauf, P. Denk, K. Forberich, M. C. Scharber, C. J. Brabec and K. Hingerl, *J. Appl. Phys.*, 2008, **103**, 084506.
146 A. K. K. Kyaw, X. W. Sun, C. Y. Jiang, G. Q. Lo, D. W. Zhao and D. L. Kwong, *Appl. Phys. Lett.*, 2008, **93**, 221107.
147 S. O'Brien, L. H. K. Koh and G. M. Crean, *Thin Solid Films*, 2008, **516**, 1391.
148 D. W. Zhao, P. Liu, X. W. Sun, S. T. Tan, L. Ke and A. K. K. Kyaw, *Appl. Phys. Lett.*, 2009, **95**, 153304.
149 J. B. Kim, C. S. Kim, Y. S. Kim and Y.-L. Loo, *Appl. Phys. Lett.*, 2009, **95**, 183301.
150 K. Takanezawa, K. Tajima and K. Hashimoto, *Appl. Phys. Lett.*, 2008, **93**, 063308.
151 J. Ouyang and Y. Yang, *Adv. Mater.*, 2006, **18**, 2141.
152 J. Huang, G. Li and Y. Yang, *Adv. Mater.*, 2008, **20**, 415.
153 V. Shrotriya, E. H.-E. Wu, G. Li, Y. Yao and Y. Yang, *Appl. Phys. Lett.*, 2006, **88**, 064104.
154 T. Oyamada, Y. Sugawara, Y. Terao, H. Sasabe and C. Adachi, *Jpn. J. Appl. Phys.*, 2007, **46**, 1734.

155 R. F. Bailey-Salzman, B. P. Rand and S. R. Forrest, *Appl. Phys. Lett.*, 2006, **88**, 233502.
156 G.-M. Ng, E. L. Kietzke, T. Kietzke, L.-W. Tan, P.-K. Liew and F. Zhu, *Appl. Phys. Lett.*, 2007, **90**, 103505.
157 J. Hanisch, E. Ahlswede and M. Powalla, *Eur. Phys. J.: Appl. Phys.*, 2007, **37**, 261.
158 F.-C. Chen, J.-L. Wu, C.-L. Lee, W.-C. Huang, H.-M. P. Chen and W.-C. Chen, *IEEE Electron Device Lett.*, 2009, **30**, 727.
159 H. Schmidt, H. Flügge, T. Winkler, T. Bülow, T. Riedl and W. Kowalsky, *Appl. Phys. Lett.*, 2009, **94**, 243302.
160 C. Tao, S. P. Ruan, G. H. Xie, X. Z. Kong, L. Shen, F. X. Meng, C. X. Liu, X. D. Zhang, W. Dong and W. Y. Chen, 2009, 94, p. 043311.
161 K. M. Coakley and M. D. McGehee, *Chem. Mater.*, 2004, **16**, 4533.
162 J. S. Huang, C.-Y. Chou, M.-Y. Liu, K.-H. Tsai, W.-H. Lin and C.-F. Lin, *Org. Electron.*, 2009, **10**, 1060.
163 W.-H. Baek, I. Seo, T.-S. Yoon, H. H. Lee, C. M. Yun and Y.-S. Kim, *Sol. Energy Mater. Sol. Cells*, 2009, **93**, 1587.
164 B. Y. Yu, A. Tsai, S. P. Tsai, K. T. Wong, Y. Yang, C.-W. Chu and J. J. Shyue, *Nanotechnology*, 2008, **19**, 255202.
165 K. M. Coakley, B. S. Srinivasan, J. M. Ziebarth, C. Goh, Y. Liu and M. D. McGehee, *Adv. Funct. Mater.*, 2005, **15**, 1927.
166 G. K. Mor, K. Shankar, M. Paulose, O. K. Varghese and C. A. Grimes, *Appl. Phys. Lett.*, 2007, **91**, 152111.
167 M. Geoghegan, *Prog. Polym. Sci.*, 2003, **28**, 261.
168 A. Budkowski, A. Bernasik, P. Cyganik, J. Raczkowska, B. Penc, B. Bergues, K. Kowalski, J. Rysz and J. Janik, *Macromolecules*, 2003, **36**, 4060.
169 J. Genzer and E. J. Kramer, *Phys. Rev. Lett.*, 1997, **78**, 4946.
170 U. Steiner, J. Klein, E. Eiser, A. Budkowski and L. J. Fetters, *Science*, 1992, **258**, 1126.
171 G. Krausch, Mater. Sci. Eng., R, 1995, **14**, v.
172 F. Bruder and R. Brenn, *Phys. Rev. Lett.*, 1992, **69**, 624.
173 C. Ton-That, A. G. Shard, D. O. H. Teare and R. H. Bradley, *Polymer*, 2001, **42**, 1121.
174 M. Böltau, S. Walheim, J. Mlynek, G. Krausch and U. Steiner, *Nature*, 1998, **391**, 877.
175 S. Y. Heriot and R. A. L. Jones, *Nat. Mater.*, 2005, **4**, 782.
176 J. Raczkowska, A. Bernasik, A. Budkowski, K. Sajewicz, B. Penc, J. Lekki, M. Lekka, J. Rysz, K. Kowalski and P. Czuba, *Macromolecules*, 2004, **37**, 7308.
177 A. C. Arias, N. Corcoran, M. Banach, R. H. Friend, J. D. MacKenzie and W. T. S. Huck, *Appl. Phys. Lett.*, 2002, **80**, 1695.
178 J. Chappell, D. G. Lidzey, P. C. Jukes, A. M. Higgins, R. L. Thompson, S. O'Connor, I. Grizzi, R. Fletcher, J. O'Brien, M. Geoghegan and R. A. L. Jones, *Nat. Mater.*, 2003, **2**, 616.
179 J.-S. Kim, P. K. H. Ho, C. E. Murphy and R. H. Friend, *Macromolecules*, 2004, **37**, 2861.
180 A. M. Higgins, S. J. Martin, R. L. Thompson, J. Chappell, M. Voigt, D. G. Lidzey, R. A. L. Jones and M. Geoghegan, *J. Phys.: Condens. Matter*, 2005, **17**, 1319.
181 J. J. M. Halls, A. C. Arias, J. D. MacKenzie, W. S. Wu, M. Inbasekaran, E. P. Woo and R. H. Friend, *Adv. Mater.*, 2000, **12**, 498.
182 A. C. Arias, J. D. MacKenzie, R. Stevenson, J. J. M. Halls, M. Inbasekaran, E. P. Woo, D. Richards and R. H. Friend, *Macromolecules*, 2001, **34**, 6005.
183 S. Goffri, C. Müller, N. Stingelin-Stutzmann, D. W. Breiby, C. P. Radano, J. W. Andreasen, R. Thompson, R. A. J. Janssen, M. M. Nielsen, P. Smith and H. Sirringhaus, *Nat. Mater.*, 2006, **5**, 950.
184 A. C. Arias, J. D. MacKenzie, R. Stevenson, J. J. M. Halls, M. Inbasekaran, E. P. Woo, D. Richards and R. H. Friend, *Macromolecules*, 2001, **34**, 6005.
185 L.-L. Chua, P. K. H. Ho, H. Sirringhaus and R. H. Friend, *Appl. Phys. Lett.*, 2004, **84**, 3400.
186 A. C. Arias, F. Endicott and R. A. Street, *Adv.Mater.*, 2006, **18**, 2900.
187 L. Z. Qiu, J. A. Lim, X. H. Wang, W. H. Lee, M. K. Hwang and K. Cho, *Adv. Mater.*, 2008, **20**, 1141.
188 G. Greczynski, T. Kugler and W. R. Salaneck, *Thin Solid Films*, 1999, **354**, 129.
189 A. M. Higgins, S. J. Martin, P. C. Jukes, M. Geoghegan, R. A. L. Jones, S. Langridge, R. Cubitt, S. Kirchmeyer, A. Wehrum and I. Grizzi, *J. Mater. Chem.*, 2003, **13**, 2814.
190 H. J. Snaith, H. Kenrick, M. Chiesa and R. H. Friend, *Polymer*, 2005, **46**, 2573.
191 L. H. Slooff, S. C. Veenstra, J. M. Kroon, D. J. D. Moet, J. Sweelssen and M. M. Koetse, *Appl. Phys. Lett.*, 2007, **90**, 143506.
192 O. Inganäs, F. L. Zhang and M. Andersson, *Acc. Chem. Res.*, 2009, **42**, 1731.
193 A. Bernasik, J. Rysz, A. Budkowski, K. Kowalski, J. Camra and J. Jedliski, *Macromol. Rapid Commun.*, 2001, **22**, 829.
194 C. M. Björström, A. Bernasik, J. Rysz, A. Budkowski, S. Nilsson, M. Svensson, M. R. Andersson, K. O. Magnusson and E. Moons, *J. Phys.: Condens. Matter*, 2005, **17**, L529.
195 C. M. Björström Svanström, J. Rysz, A. Bernasik, A. Budkowski, F. L. Zhang, O. Inganäs, M. R. Andersson, K. O. Magnusson, J. J. Benson-Smith, J. Nelson and E. Moons, *Adv. Mater.*, 2009, **21**, 4398.
196 G. Dennler, H.-J. Prall, R. Koeppe, M. Egginger, R. Autengruber and N. S. Sariciftci, *Appl. Phys. Lett.*, 2006, **89**, 073502.
197 H.-J. Prall, R. Koeppe, R. Autengruber, M. Egginger, G. Dennler and N. S. Sariciftci, in *Proc. of the Soc. of Photo-Optical Instrumentation Engineers*, ed. A. Gombert, SPIE, Bellingham, WA, 2006, p. F1970.
198 S. Nilsson, A. Bernasik, A. Budkowski and E. Moons, *Macromolecules*, 2007, **40**, 8291.
199 L. M. Andersson and O. Inganäs, *Appl. Phys. Lett.*, 2006, **88**, 082103.
200 V. D. Mihailetchi, L. J. A. Koster, P. W. M. Blom, C. Melzer, B. de Boer, J. K. J. van Duren and R. A. J. Janssen, *Adv. Funct. Mater.*, 2005, **15**, 795.
201 L. M. Andersson, F. Zhang and O. Inganäs, *Appl. Phys. Lett.*, 2007, **91**, 071108.
202 H. Hoppe, T. Glatzel, M. Niggemann, A. Hinsch, M. C. Lux-Steiner and N. S. Sariciftci, *Nano Lett.*, 2005, **5**, 269.
203 C. M. Björström, S. Nilsson, A. Bernasik, A. Budkowski, M. Andersson, K. O. Magnusson and E. Moons, *Appl. Surf. Sci.*, 2007, **253**, 3906.
204 A. J. Moulé and K. Meerholz, *Adv. Mater.*, 2008, **20**, 240.
205 J. K. Lee, W. L. Ma, C. J. Brabec, J. Yuen, J. S. Moon, J. Y. Kim, K. Lee, G. C. Bazan and A. J. Heeger, *J. Am. Chem. Soc.*, 2008, **130**, 3619.
206 Y. Yao, J. H. Hou, Z. Xu, G. Li and Y. Yang, *Adv. Funct. Mater.*, 2008, **18**, 1783.
207 C. S. Kim, L. L. Tinker, B. F. Disalle, E. D. Gomez, S. Lee, S. Bernhard and Y.-L. Loo, *Adv. Mater.*, 2009, **21**, 3110.
208 K. Ohno and Y. Kawazoe, *Scr. Mater.*, 2001, **44**, 1579.
209 R. J. Kline, D. M. DeLongchamp, D. A. Fischer, E. K. Lin, M. Heeney, I. McCulloch and M. F. Toney, *Appl. Phys. Lett.*, 2007, **90**, 062117.
210 D. S. Germack, C. K. Chan, B. H. Hamadani, L. J. Richter, D. A. Fischer, D. J. Gundlach and D. M. DeLongchamp, *Appl. Phys. Lett.*, 2009, **94**, 233303.
211 M. P. Felicissimo, D. Jarzab, M. Gorgoi, M. Forster, U. Scherf, M. C. Scharber, S. Svensson, P. Rudolf and M. A. Loi, *J. Mater. Chem.*, 2009, **19**, 4899.
212 W. Ma, C. Y. Yang and A. J. Heeger, *Adv. Mater.*, 2007, **19**, 1387.
213 M. Y. Chiu, U. S. Jeng, C. H. Su, K. S. Liang and K. H. Wei, *Adv. Mater.*, 2008, **20**, 2573.
214 X. Yang, J. Loos, S. C. Veenstra, W. J. H. Verhees, M. M. Wienk, J. M. Kroon, M. A. J. Michels and R. A. J. Janssen, *Nano Lett.*, 2005, **5**, 579.
215 S. van Bavel, E. Sourty, G. de With and J. Loos, *Nano Lett.*, 2009, **9**, 507.
216 X. Yang, J. K. J. van Duren, R. A. J. Janssen, M. A. J. Michels and J. Loos, *Macromolecules*, 2004, **37**, 2151.
217 H. Hoppe, M. Drees, W. Schwinger, F. Schaffler and N. S. Sariciftci, *Synth. Met.*, 2005, **152**, 117.
218 H. Hoppe, M. Niggemann, C. Winder, J. Kraut, R. Hiesgen, A. Hinsch, D. Meissner and N. S. Sariciftci, *Adv. Funct. Mater.*, 2004, **14**, 1005.
219 H. Hoppe and N. S. Sariciftci, *J. Mater. Chem.*, 2006, **16**, 45.
220 S. S. van bavel, E. Sourty, G. de With, V. S and J. Loos, *J. Mater. Chem.*, 2009, **19**, 5388.
221 S. van Bavel, E. Sourty, G. de With, K. Frolic and J. Loos, *Macromolecules*, 2009, **42**, 7396.

222 B. V. Andersson, A. Herland, S. Masich and O. Inganäs, *Nano Lett.*, 2009, **9**, 853.
223 M. G. Harrison, J. Gruner and G. C. W. Spencer, *Phys. Rev. B: Condens. Matter*, 1997, **55**, 7831.
224 A. C. Arias, *Polym. Rev.*, 2006, **46**, 103.
225 F.-C. Chen, Y. K. Lin and C.-J. Ko, *Appl. Phys. Lett.*, 2008, **92**, 023307.
226 Q. Wei, T. Nishizawa, K. Tajima and K. Hashimoto, *Adv. Mater.*, 2008, **20**, 2211.
227 D. R. Iyengar, S. M. Perutz, C.-A. Dai, C. K. Ober and E. J. Kramer, *Macromolecules*, 1996, **29**, 1229.
228 S. Yamakawa, K. Tajima and K. Hashimoto, *Org. Electron.*, 2009, **10**, 511.
229 F.-C. Chen and S.-C. Chien, *J. Mater. Chem.*, 2009, **19**, 6865.
230 M. Granström, K. Petritsch, A. C. Arias, A. Lux, M. R. Andersson and R. H. Friend, *Nature*, 1998, **395**, 257.
231 T.-F. Guo, S. Pyo, S.-C. Chang and Y. Yang, *Adv. Funct. Mater.*, 2001, **11**, 339.
232 M. Nakamura, C. H. Yang, K. Tajima and K. Hashimoto, *Sol. Energy Mater. Sol. Cells*, 2009, **93**, 1681.
233 M. Drees, K. Premaratne, W. Graupner, J. R. Heflin, R. M. Davis, D. Marciu and M. Miller, *Appl. Phys. Lett.*, 2002, **81**, 4607.
234 M. Drees, R. M. Davis and J. R. Heflin, *Phys. Rev. B: Condens. Matter Mater. Phys.*, 2004, **69**, 165320.
235 M. Drees, R. M. Davis and J. R. Heflin, *J. Appl. Phys.*, 2005, **97**, 036103.
236 T. A. M. Ferenczi, G. J. Nelson, C. Belton, A. M. Ballantyne, M. Campoy-Quiles, F. M. Braun and D. D. C. Bradley, *J. Phys.: Condens. Matter*, 2008, **20**, 475203.
237 A. Fujii, H. Mizukami, T. Umeda, T. Shirakawa, Y. Hashimoto and K. Yoshino, *Jpn. J. Appl. Phys.*, 2004, **43**, 8312.
238 D. H. Wang, H. K. Kee, D.-G. Choi, J. H. Park and O. O. Park, *Appl. Phys. Lett.*, 2009, **95**, 043505.
239 M. Shakutsui, T. Iwamoto, R. Maeda, T. Tsutsui and K. Fujita, *Proc. SPIE*, 2008, **7052**, 705215.
240 F. A. Castro, H. Benmansour, C. F. O. Graeff, F. Nüesch, E. Tutis and R. Hany, *Chem. Mater.*, 2006, **18**, 5504.
241 A. Kumar, G. Li, Z. R. Hong and Y. Yang, *Nanotechnology*, 2009, **20**, 165202.
242 B. Sun, H. J. Snaith, A. S. Dhoot, S. Westenhoff and N. C. Greenham, *J. Appl. Phys.*, 2005, **97**, 014914.
243 J. Hwang, A. Wan and A. Kahn, *Mater. Sci. Eng., R*, 2009, **64**, 1.
244 S. Braun, W. R. Salaneck and M. Fahlman, *Adv. Mater.*, 2009, **21**, 1450.
245 A. S. Wan, J. Hwang, F. Amy and A. Kahn, *Org. Electron.*, 2005, **6**, 47.
246 C. Tengstedt, W. Osikowicz, W. R. Salaneck, I. D. Parker, Che-H. Hsu and M. Fahlman, *Appl. Phys. Lett.*, 2006, **88**, 053502.
247 Z. Xu, L.-M. Chen, M.-H. Chen, G. Li and Y. Yang, *Appl. Phys. Lett.*, 2009, **95**, 013301.
248 F. J. Zhang, A. Vollmer, J. Zhang, Z. Xu, J. P. Rabe and N. Koch, *Org. Electron.*, 2007, **8**, 606.
249 Y. D. Park, J. H. Cho, D. H. Kim, Y. Jang, H. S. Lee, K. Ihm, T.-H. Kang and K. Choc, *Electrochem. Solid-State Lett.*, 2006, **9**, G317.
250 W. Osikowicz, M. P. de Jong and W. R. Salaneck, *Adv. Mater.*, 2007, **19**, 4213.
251 S. Braun, W. Osikowicz, Y. Wang and W. R. Salaneck, *Org. Electron.*, 2007, **8**, 14.
252 K. Akaike, K. Kanai, H. Yoshida, J. Tsutsumi, T. Nishi, N. Sato, Y. Ouchi and K. Seki, *J. Appl. Phys.*, 2008, **104**, 023710.
253 N. R. Armstrong, W. Wang, D. M. Alloway, D. Placencia, E. Ratcliff and M. Brumbach, *Macromol. Rapid Commun.*, 2009, **30**, 717.
254 R. J. Murdey and W. R. Salaneck, *Jpn. J. Appl. Phys.*, 2005, **44**, 3751.
255 S. Braun, M. P. de Jong, W. Osikowicz and W. R. Salaneck, *Appl. Phys. Lett.*, 2007, **91**, 202108.
256 C.-P. Chen, T.-C. Tien, B.-T. Ko, Y.-D. Chen and C. Ting, *ACS Appl. Mater. Interfaces*, 2009, **1**, 741.
257 A. Lachkar, A. Selmani, E. Sacher, M. Leclerc and R. Mokhliss, *Synth. Met.*, 1994, **66**, 209.
258 A. Lachkar, A. Selmani and E. Sacher, *Synth. Met.*, 1995, **72**, 73.
259 R. P. Mikalo and D. Schmeisser, *Synth. Met.*, 2002, **127**, 273.
260 W. Zhao, Y. Guo, X. Feng, L. Zheng, W. Zhang and J. Zhu, *Chin. Sci. Bull.*, 2009, **54**, 1978.
261 J. Zhu, F. Bebensee, W. Hieringer, W. Zhao, J. H. Baricuatro, J. A. Farmer, Y. Bai, H.-P. Steinrück, J. M. Gottfried and C. T. Campbell, *J. Am. Chem. Soc.*, 2009, **131**, 13498.

